

Hardening and Strain Localisation in Helium-Ion-Implanted Tungsten

Suchandrima Das^a, Hongbing Yu^a, Edmund Tarleton^b, Felix Hofmann^{a*}

^a*Department of Engineering Science, University of Oxford, Parks Road, Oxford OX1 3PJ, UK*

^b*Department of Materials, University of Oxford, Parks Road, Oxford OX1 3PH, UK*

*felix.hofmann@eng.ox.ac.uk

Keywords: tungsten; nano-indentation; micro-beam Laue diffraction; crystal-plasticity; helium-implantation

ABSTRACT

Tungsten is the main candidate material for plasma-facing armour components in future fusion reactors. In service, bombardment with energetic neutrons will create collision cascades that leave behind lattice defects. Helium, injected from the plasma and produced by transmutation, strongly interacts with these defects, modifying their behaviour and retention. Helium-ion-implantation provides an effective tool for examining helium-defect interactions and their effect on the properties of tungsten armour. We use nano-indentation to probe the mechanical properties of the shallow helium-ion-implanted layer. Comparison of spherical indents in unimplanted and helium-implanted regions of the same single crystal shows a large increase in hardness and substantial pile-up in the implanted material. The complex lattice distortions beneath indents are probed non-destructively using 3D-resolved synchrotron X-ray micro-diffraction. Reduced lattice rotations and indentation-induced residual strains in the ion-implanted material indicate a more confined plastic zone. This is confirmed by HR-EBSD and TEM observations. Together our results suggest that dislocation motion is initially obstructed by helium-induced defects. The obstacle strength of these defects is reduced by the passage of dislocations, leading to a strain-softening and slip channel formation. A constitutive law for 3D crystal plasticity finite element simulations is developed based on this

hypothesis. Simulations of the indentation process successfully capture the helium-implantation induced changes in deformation behaviour observed in experiments. Importantly, the effects we observe are markedly different from previous observations for self-ion-implanted tungsten, highlighting that the exact nature of the implantation damage plays a critical role in determining mechanical property change.

1. INTRODUCTION

There is an ongoing search for plasma facing armour materials for critical components in future fusion reactors, such as the main wall and the divertor. Tungsten is a promising candidate due to its high melting point, reasonable strength at high temperatures and low sputtering yield [1–3]. Within the fusion reactor, armour components will be bombarded with high energy neutrons (14.2 MeV, ~2 dpa per year for tungsten) and exposed to high temperatures (>1200 K) [3,4]. Foreign elements like hydrogen and helium will accumulate within initially pure tungsten components due to transmutation and migration from the fusion plasma [4]. The presence of helium in tungsten is particularly worrying because of its low solubility and strong affinity for lattice defects [5,6]. It aggravates the neutron damage by enhancing defect retention, causing increased hardness and reduced thermal diffusivity [7,8]. Understanding the underlying mechanisms governing the helium-defect interactions is necessary for control and prevention of these helium-induced alterations in tungsten and for accurately predicting the evolution of structural and functional properties. This in turn is key for estimating the performance and lifetime of tungsten armour components, a critical aspect for the successful design and operation of commercially viable fusion reactors.

Recreating the internal environment of the fusion reactor is not yet possible. Helium-implantation offers a good alternative for introducing irradiation-damage-like defects into the material and studying their interaction with the injected helium. Surprisingly, high-

resolution Transmission Electron Microscopy (TEM) micrographs of 0.3 at.% helium-implanted samples showed no visible damage [7], but a 30% increase in hardness [9,10] and 50% lower thermal diffusivity (at room temperature) [8] were observed. This suggests that helium-implantation-induced defects, though too small to be clearly resolved by TEM [11], are sufficiently strong to obstruct dislocation motion, causing substantial increase in hardness.

The changes in the mechanical properties of helium-implanted tungsten are accompanied by notable changes in the morphology of indents. A study by Beck et al. showed large pile-up around 250 nm deep Berkovich indents in 0.3 at.wt.% helium-implanted tungsten [9]. Recently, another experimental study showed scanning electron microscopy (SEM) micrographs of ~500 nm deep spherical indents in (001) oriented 3000 appm helium-implanted tungsten, with distinct slip steps and strikingly large pile up (~180 nm) [10]. In both cases, the unimplanted samples showed a much shallower pile-up around indents. Differences between pure and implanted tungsten are not restricted to the visible surface features. 3D resolved micro-beam Laue diffraction measurement of residual lattice distortions near these indents has shown a significantly smaller deformation zone beneath indents in the implanted sample [10].

In a similar manner to helium, self-ion implantation in tungsten also causes increased hardness; a ~20% increase in hardness was measured in 0.07 dpa self-ion implanted W-5wt%Ta [12]. The rate of increase in hardness was found to slow down with increasing damage level and finally saturate beyond 13 dpa. However, surprisingly, unlike in helium-implantation, a suppression of pile-up (< 30 nm) was seen around nano-indents in self-ion implanted samples [12].

This implies that helium-ion-implantation-induced defects have a unique effect on the deformation behaviour of tungsten due to a defect microstructure dissimilar to that formed during self-ion implantation. Self-ion implantation has been found to cause the formation of prismatic dislocations loops with a Burgers vector of predominantly $\frac{1}{2}\langle 111 \rangle$ type [13]. These loops, formed by aggregation of self-interstitial atoms (SIAs) or vacancies, can only grow or shrink via climb, requiring absorption of more point defects. The gliding dislocations require additional stress to cut through these prismatic loops, which cannot be easily removed. In contrast, helium interacts differently with the tungsten matrix. Simulations and experiments have shown that point defects, particularly vacancies can trap the otherwise very mobile helium [6,14]. Most of the numerous Frenkel pairs formed by helium implantation recombine almost immediately. Helium though, being in plentiful supply, binds to some of the vacancies and prevents a small fraction of the Frenkel pairs from recombining. An important question concerns the fate of the SIAs. Recent DFT calculations and experiments showed that the SIAs remain near to and form a stable configuration with the helium-filled vacancies [14–16].

We hypothesize that initially helium-defects strongly obstruct dislocation motion causing the observed pronounced hardening. As deformation progresses, gliding dislocations help to recombine helium-filled Frenkel defects, facilitating easier glide of subsequent dislocations through defect-free channels and creating the slip steps seen near nano-indentations in the implanted material [10]. To test this hypothesis, we examine the lattice distortions, morphology and defects near specific indentations using SEM, atomic force microscopy (AFM), high-resolution electron back-scattered diffraction (HR-EBSD), TEM, and 3D Laue diffraction [10]. Experimental observations are compared with crystal plasticity finite element (CPFE) simulations, where the interaction of mobile dislocations with helium-defects is accounted for using a physically-based constitutive law. The spatial distribution of

geometrically necessary dislocations (GNDs) beneath indents is calculated from both simulated and experimentally observed lattice distortions and evaluated as an indicator of the extent of plastic deformation. The results are discussed in light of the proposed mechanism for the interaction of helium-implantation-induced defects and glide dislocations in tungsten.

2. METHODS

2.1. Sample Preparation

A 2.5 mm radius, 0.8 mm thick disc with [001] out-of-plane orientation was cut from a tungsten single crystal (99.99% purity). A high-quality surface finish was obtained by mechanical grinding, polishing with diamond paste and final chemo-mechanical polishing with 0.1 μm colloidal silica suspension.

2.2. Helium Implantation

Implantation was done at the National Ion Beam Centre, University of Surrey, UK. The sample was partly implanted with helium at 298 K, using a 2 MeV ion accelerator, and a raster scanned beam, to ensure a uniform implantation dose. Using a combination of different ion energies and fluences (Appendix A), a near uniform helium ion concentration of ~ 3000 appm within a ~ 2.8 μm thick implanted layer was obtained [15,17,18]. The SRIM estimated implantation profile [19] (displacement energy of 68 eV, single-layer calculation model [20]) is shown in Figure 1 (a). A helium ion concentration of $\sim 3100 \pm 410$ appm, with an associated damage of 0.20 ± 0.03 displacements per atom (dpa) was obtained between 0-2.8 μm depth. Frenkel pair formation is the main damage mechanism, since helium implantation induced recoils at energies < 2 MeV have predominantly low energy [15]. Little defect clustering is expected, given the low mobility of vacancies at room temperature [7,21–23].

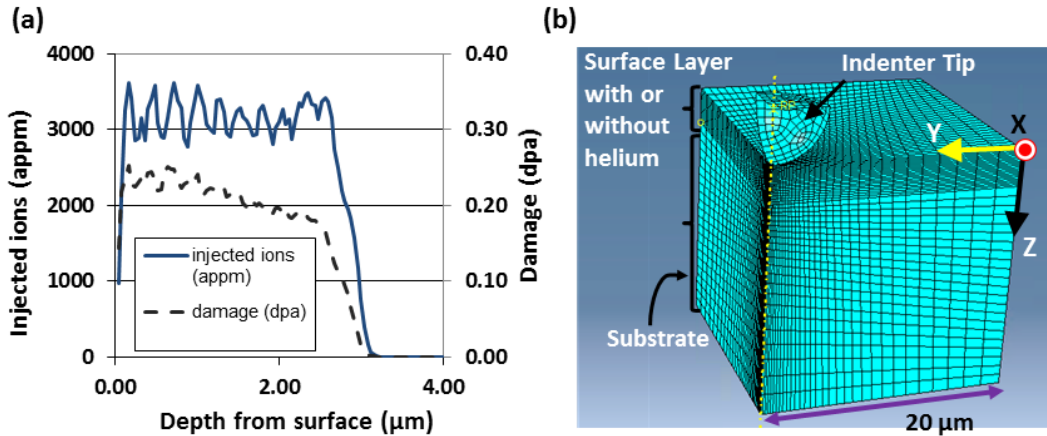


Figure 1 - (a) Helium-implantation profile as estimated by the SRIM code. (b) Refined mesh for the 3D crystal plasticity finite element simulation of the tungsten sample indented by a 4.2 μm radius spherical indenter with the X, Y, Z coordinate frame superimposed.

2.3. Nano-Indentation, AFM & SEM

Nano-indentation was performed on a MTS NanoXp, with a spherical diamond tip (~ 4.2 μm radius, 90° cone angle, from Synton MDP) to a maximum displacement of 500 nm with 50 μm spacing between indents. The indent impressions were imaged using a Zeiss Merlin FEG SEM. The surface morphology was determined using a Digital Instruments Dimension 3100 AFM in contact mode using Bruker CONTV-A tips (nominal tip radius 10 nm).

2.4. Micro-beam Laue diffraction

X-ray micro-diffraction was carried out at beamline 34-ID-E, Advanced Photon Source, Argonne National Lab, USA. A polychromatic X-ray beam (7-30 keV) was focused by KB mirrors to a sub-micron probe spot (500 nm (vertical) × 400 nm (horizontal) full width at half maximum near Lorentzian shape). With the sample placed at the probe focus in 45° reflection geometry, diffraction patterns were recorded on an area detector (Perkin-Elmer, #XRD 1621, with pixel size 200×200 μm) placed ~511 mm above the sample.

The recorded images correspond to the total intensity scattered by the entire volume illuminated by the incident beam. The depth along the incident beam from which a specific

diffraction signal originated is thus unknown. At 34-ID-E, use of the Differential Aperture X-ray Microscopy (DAXM) technique enables depth-resolved measurements. Here, a platinum wire is scanned in small steps between the detector and the diffracting sample. The depth vs intensity profile for each detector pixel is recovered by subtracting the diffraction images from consecutive wire position increments and triangulating using the wire edge and the line of the incident beam. A detailed description of the DAXM technique and the 34-ID-E instrument is given elsewhere [24–26]. For the present sample, material up to 20 μm beneath the ion-implanted surface was measured with 0.5 μm 3D spatial resolution. Laue diffraction patterns containing 30+ peaks were indexed and fitted using the LaueGo software package (J.Z. Tischler: tischler@anl.gov) to extract both lattice orientation and the full deviatoric lattice strain tensor at each measured point in 3D space.

2.5. FIB Lift-out, HR-EBSD & TEM

Focused ion beam (FIB) lift-out cross-section samples ($\sim 3 \mu\text{m}$ thick) were made from the indent-centre in the implanted and unimplanted samples using a Zeiss Auriga FIB-SEM. For HR-EBSD measurements, lift-outs were thinned from one side to $\sim 1.5 \mu\text{m}$ thickness using a 30 kV, 240 pA ion beam, followed by low energy ion beam polishing (2 kV, 200 pA, 10 minutes) to remove FIB damage. For TEM characterization, the lift-out specimens were further thinned to $\sim 100 \text{ nm}$ using FIB, and then flash polished (1% NaOH aqueous solution, 0.05 s, 8 V, 298 K). Though the FIB lift-out preparation removes constraints perpendicular to the foil, the in-plane lattice strains and rotations are expected to remain largely unchanged and can be compared to those measured by Laue diffraction and predicted by CPFEM.

HR-EBSD measurements were performed on a Zeiss Merlin FEG SEM equipped with a Bruker eFlash detector. With a configuration similar to EBSD, in HR-EBSD the Kikuchi pattern at each point is recorded at the full detector resolution. HR-EBSD can measure the 2D spatial variation of lattice distortions by cross-correlating the EBSD pattern collected at each

point in a map with a pattern collected at a nominally strain-free reference position [27–29]. From this the deviatoric lattice strain ($\sim 1 \times 10^{-3}$) and lattice rotation ($\sim 1 \times 10^{-3}$ rads) for each point can be found [30–32]. Next the elastic deformation gradient can be computed [30] and hence the geometrically necessary dislocation (GND) density estimated [33]. Here the nominally undistorted reference point was chosen far away from the indent ($>10 \mu\text{m}$) in the unimplanted substrate material. Analysis of the Kikuchi patterns was carried out using the XEBSD code provided by A. J. Wilkinson [30].

TEM characterization was performed on a JEOL 2100 TEM at 200 keV. The TEM micrographs were taken under a two-beam bright field condition.

2.6. CPFE Modelling

A strain-gradient CPFE model was used to simulate the indentation experiments. The advantage of CPFE is that plastic deformation is constrained to occur only in directions consistent with crystallographic slip. A 3D model consisting of a $20 \times 20 \times 20 \mu\text{m}^3$ deformable block and a rigid $4.2 \mu\text{m}$ radius spherical indenter was simulated using Abaqus 2016 (Dassault Systèmes, Providence, RI, USA), as shown in Figure 1(b). Using symmetry, only one quarter of the experimental setup was simulated, and mirror boundary conditions were applied on the XZ and YZ planes. The top surface was traction free and the remaining surfaces of the sample block were fixed. Additional boundary conditions, included for the helium-implanted tungsten, are explained in Section 2.6.2.

The sample block was assigned elastic properties of tungsten and the indenter was approximated as a discrete rigid wire frame. Since the stiffness of tungsten (sample) is a significant fraction ($\sim 36\%$) of diamond (indenter tip), the results were scaled with an effective modulus E_{eff} to account for the indenter tip compliance (details in Appendix B) [34]. Contact between the sample and indenter was defined using the Abaqus node to surface

contact algorithm and the indenter was subjected to a displacement of 0.5 μm into the sample block before unloading. A refined finite element mesh (applied edge bias 0.1 to 2 μm) with 39500, 20-noded, reduced integration (8 integration points) 3D quadratic elements (C3D20R) was used as shown in Fig. 1 (b).

Crystal plasticity was implemented using a user material subroutine (UMAT) that shares data between gauss points using a common block. Recently we successfully demonstrated the use of strain-gradient CPFE for performing 3D simulations of nano-indentation in pure tungsten [33]. The predicted residual lattice distortions beneath indents were in good agreement with the corresponding micro-beam Laue diffraction measurements. Here, we use a modified version of this UMAT to simulate nano-indentation in helium-implanted tungsten.

The crystal plasticity framework used here is based on the method of decomposing the deformation gradient (\mathbf{F}) into elastic and plastic tensors [33,35]. Fundamental equations for this framework are given in Appendix C and a detailed description can be found in [33]. The UMAT code is based on the user element (UEL) originally developed by Dunne et al. [36].

Within this framework, a physically based slip law [36] was used to approximate the crystallographic slip rate $\dot{\beta}^{\lambda}$ for each slip system λ , by considering the thermally activated glide of dislocations in a field of pinning dislocations

$$\dot{\beta}_p^{\lambda}(\tau^{\lambda}) = \rho_m \nu (b^{\lambda})^2 \exp\left(-\frac{\Delta F}{kT}\right) \sinh\left(\frac{\text{sgn}(\tau^{\lambda})(|\tau^{\lambda}| - \tau_c)V}{kT}\right) \quad (1)$$

where, ρ_m is the density of mobile dislocations, ν the attempt frequency, b^{λ} the Burgers vector magnitude, ΔF the Helmholtz free energy, k the Boltzmann constant, T the temperature in Kelvin, τ_c the critically resolved shear stress (considered the same for all slip-systems), τ^{λ} the resolved shear stress on slip system λ and V the activation volume, which depends on the spacing between the pinning dislocations l . We assume

$l = \frac{1}{\sqrt{\Psi(\rho_{SSD})}}$, where, coefficient Ψ represents the probability of pinning and ρ_{SSD} is the density of statistically stored dislocations (SSD). Values of the UMAT parameters (acquired from literature, fitted to experimental results or physically based) are listed in Appendix C. Isotropic elasticity and small elastic deformations were assumed in the numerical simulation. It is to be noted that for simplicity all parameters on the RHS in Eq. (1) are assumed constant, other than τ_c (and the independent variable τ^λ).

Lattice rotations and residual elastic strain fields beneath the indents were extracted from the CPFE simulations and compared to the corresponding experimental measurements. The model was constructed with the same initial crystallographic orientation as the physical sample. All experimental and simulated results are presented in the same sample coordinate frame and using the same colour and length scales to facilitate a direct comparison.

2.6.1. Fitting Parameters for the UMAT

GNDs are generated to accommodate lattice curvature during plastic deformation. To account for strain hardening, a Taylor hardening law was used [37,38]. The CRSS, τ_c , is updated at the end of each time increment by $C'G b \sqrt{\rho_{GND}}$, where C' is a hardening factor fitted to the experimental data, G the shear modulus of tungsten and ρ_{GND} the sum of the GNDs produced across all slip-systems.

$$\tau_c = \tau_c^0 + C'G b \sqrt{\rho_{GND}} \quad (2)$$

Only two UMAT parameters, the initial critically resolved shear stress (CRSS), τ_c^0 , and the hardening coefficient, C' , due to GNDs were fitted to the experimental nano-indentation load-displacement curve and indent surface profile of the unimplanted sample. The 20 μm high simulation block was partitioned into two layers: a 3 μm thick implanted layer at the free surface and a 17 μm thick substrate. When simulating indentation of the unimplanted material, both layers of the block were assigned identical material properties

including the two fitting parameters C' and τ_c^0 . To simulate the helium-implanted sample, the 17 μm thick substrate was left unaltered and the implanted layer was assigned these material parameters along with two additional parameters to account for the presence of helium-induced defects as described below (section 2.6.2 and Appendix C).

2.6.2. CPFE Formulation for Helium-implanted tungsten

The UMAT formulation is based on the observation that helium-implantation leads to increased hardness, a confined deformation zone and slip step formation during nano-indentation of tungsten [10]. We hypothesize that helium-induced defects initially act as strong obstacles to gliding dislocations. However, the strength of these obstacles is reduced by the passage of dislocations, leading to the formation of channels with reduced defect density.

To capture the physics of this mechanism in the UMAT formulation, we applied a strain softening effect in the helium-implanted layer. For this layer, an additional term is included in Eq. (2) for updating the CRSS. The additional term corresponds to the shear stress resulting from the helium τ_H (with initial value τ_H^0 at $t = 0$) to account for the increased resistance to dislocation glide by the helium-implantation-induced defects. The equation for this layer is

$$\tau_c = \tau_c^0 + C' G b \sqrt{\rho_{GND}} + \tau_H \quad (3)$$

Strain-softening, due to removal of helium-defects, is implemented by reducing τ_H at the end of each time increment, as a function of accumulated crystallographic slip, β_p :

$$\beta_p^{t+\Delta t} = \beta_p^t + \sum_{\lambda=1}^n \dot{\beta}_p^\lambda \Delta t \quad (4)$$

$$\tau_H^{t+\Delta t} = \tau_H^0 e^{-(\beta_p^{t+\Delta t}/\gamma)} \quad (5)$$

where Δt is the time increment, β_p^t and $\beta_p^{t+\Delta t}$ are the accumulated crystallographic summed over all slip systems at the start and end of the increment. The γ parameter here controls the softening rate and is fitted to the experimental load-displacement curve of the implanted sample.

Prior studies show that an increase in pile-up and slip step formation occur when the stress required to expand a slipped area reduces with increasing slip, i.e. there is a softening [39]. Here, in the helium-implanted material, dislocation glide is resisted by τ_H and τ_c (for maximum helium-defect concentration $\tau_H^0 \approx 2\tau_c^0$ dominates). The large pile-up and slip steps seen experimentally may be caused by a rapid fall in the dominant resistance force τ_H in defect-reduced channels with an associated increase in slip rate. The rate of decrease of τ_H can be estimated to be proportional to its current value i.e. the current helium defect concentration¹. This suggests an exponential softening rate as a function of $\beta_p^{t+\Delta t}$ as chosen in Eq. (5). We note that, of the two parameters in this model, only γ is fitted to the experimental data.

To determine τ_H^0 a slip-plane interspersed with helium-defects is considered (Figure C.1). In Figure C.1, each circle represents a defect (helium-vacancy cluster with SIA attached to it [15]), separated from each other by a spacing L and resisting dislocation glide with force F_s . Thus, in order to glide, the force per unit length required on the dislocation must be

$$\tau_H^0 b = \frac{F_s}{L} \quad (6)$$

An area L^2 of the slip plane contains one defect. This area also contains $(L/b)^2$ atoms in total, so knowing defect concentration c Eq. (6) can be re-written as

¹ $\left. \frac{\partial \tau_H}{\partial \beta_p} \right|_{t+\Delta t} = \tau_H(\beta_p^{t+\Delta t})/\gamma$

$$\tau_H^0 = \frac{F_S}{bL} = \frac{F_S\sqrt{c}}{b^2} \quad (7)$$

The force F_S may be considered a function of the energy required for the dissociation of the helium-vacancy clusters constituting the defects i.e.

$$2r_W F_S \approx \Delta E \quad (8)$$

where, ΔE is the dissociation energy and r_W the atomic radius. The helium-vacancy cluster, primarily involving nearest neighbours [16], is estimated to be twice the size of the atomic radius of tungsten. Based on ab-initio studies of the stability of small helium-vacancy clusters, ΔE is estimated to be approximately 2.5 eV [40]. Given the helium-implantation dose of 3000 appm, the concentration of defects, c , is estimated as 1.5×10^{-3} (assuming on average 2 helium atoms per Frenkel pair) [15]. Knowing the values of b , ΔE , r_W (135 pm [41]) and c , τ_H^0 can be estimated as

$$\tau_H^0 = \frac{\Delta E\sqrt{c}}{2r_W b^2} = 750 \text{ MPa} \quad (9)$$

Additional stress boundary conditions, σ_{xx}^{BC} and σ_{yy}^{BC} , are applied to the helium-implanted layer to account for the restricted displacement in the X and Y directions (coordinates shown in Figure 1 (b)) required to maintain geometrical continuity between the implanted layer and substrate [42]. 3000 appm of helium implantation, at 300 °C, in tungsten and tungsten-1 at.wt.% rhenium alloys has been found to cause a large out-of-plane lattice strain, $\varepsilon_{zz} \approx 1400 \times 10^{-6}$ with associated in-plane stresses $\sigma_{xx}^{BC} = \sigma_{yy}^{BC} \approx -410$ MPa due to boundary conditions [15,42]. In the present sample ε_{zz} , estimated from the Laue measurements of deviatoric strain, has a slightly lower magnitude, $\varepsilon_{zz} \approx 825 \times 10^{-6}$, resulting in $\sigma_{xx}^{BC} = \sigma_{yy}^{BC} \approx -260$ MPa (calculations provided in Appendix C).

3. RESULTS & DISCUSSION

3.1. Load-displacement curves, indent morphology and defect structures

Figure 2 (c) shows the load versus displacement curves for both samples as measured by nano-indentation and predicted by CPFGE. The agreement is surprisingly good. Both CPFGE and experiment show the implanted sample reaching $\sim 73\%$ higher load than the unimplanted sample. This substantial increase in hardening may be attributed to both the helium-defects, as well as the increase in pile-up, with an associated increase in contact area.

It is interesting to compare the CPFGE predicted load-displacement curves for the implanted material with and without the implantation-induced stress boundary conditions (see section 2.6.2), keeping all other UMAT parameters the same. The indentation load predicted without the residual stresses is $\sim 16\%$ lower than the experimental observation. This suggests that large residual stresses (here $\sim 75\%$ of τ_c^0) must be accounted for to yield accurate results. Prior studies on hardness of mild steel, probed through micro-indentation, showed a similar dependence on residual stress state [43]. Interestingly our CPFGE calculations highlight that the impact of residual stress on indentation response continues to be important even at the nano-scale.

Figure 2 (a)-(b) show SEM micrographs of the indents in the unimplanted and implanted sample respectively. In striking contrast to the unimplanted sample, a large, localised pile up is seen around the indent in the implanted material. Black arrows in Figure 2 (b) indicate slip steps, suggestive of slip localisation and slip channel formation. The TEM micrograph of the cross-section from the implanted materials' indent centre (Figure 2 (d)) confirms the presence of clear defect free zones, supporting the hypothesis of defect removal by glide dislocations, on which the CPFGE formulation is based.

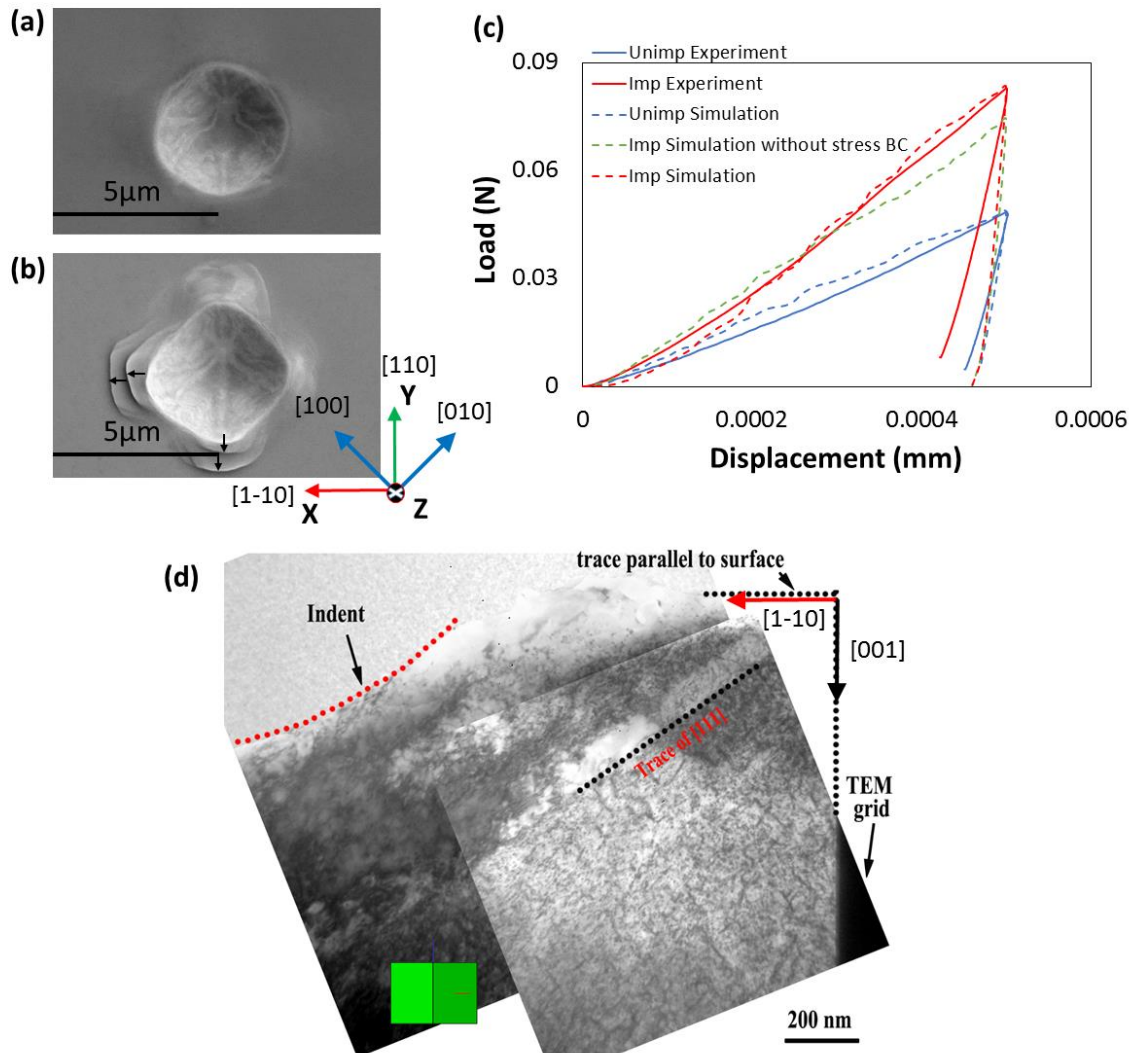


Figure 2 – (a) and (b) show SEM micrographs of the nano-indent made with a $4.2\ \mu\text{m}$ radius spherical indenter tip in the unimplanted and the helium-implanted sample, respectively. The X, Y and Z axes are superimposed. (c) Load versus displacement curve for the unimplanted and helium-implanted tungsten sample as obtained from nano-indentation and predicted by CPFE. (d) TEM micrograph of the FIB-lift-out cross-section from the indent-centre in the implanted sample, showing the presence of slip channels beneath the indent. The green cube represents the crystal orientation of the TEM lamella, also indicated by red (X axis) and black (Z axis) arrows showing the same coordinate frame as in (a).

Microscopically localized deformation through slip channel formation was initially observed in neutron-irradiated fcc single crystal copper [44]. Similar to these observations, here too the slip channels are found to be parallel to the [111] direction and cleared of almost all visible defects. However, slip channels in neutron-irradiated copper [39,44], self-ion irradiated

stainless steel [45,46], or neutron-irradiated pure Fe [47], all appear much more clearly demarcated, with sharp boundaries. In contrast, the slip channels we observe have a less well-defined boundary with the surrounding, higher defect density material. This observation is similar to 0.12 dpa neutron-irradiated bcc vanadium [48]. In vanadium channeling increased with damage level, with wider, river-pattern shaped channels forming in 0.69 dpa irradiated material [49]. Stacking fault energy (SFE) plays a key role in controlling the mechanism of strain localization [50], and the high SFE of bcc metals [51] may explain the observed differences in the slip channels morphology between bcc and fcc metals.

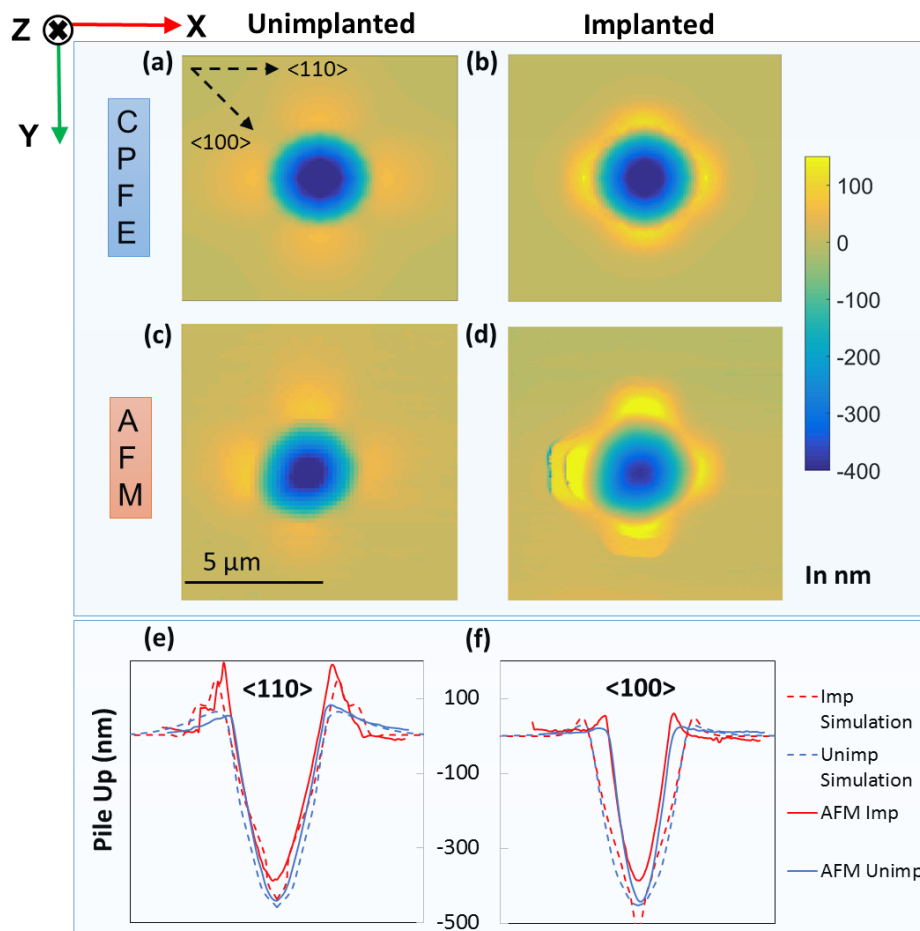


Figure 3 – Surface profiles of the nano-indentations; (a) and (b) as obtained through CPFE formulation for the unimplanted and the helium-implanted tungsten sample respectively, (c) and (d) as obtained through AFM measurements for the unimplanted and helium-implanted tungsten sample respectively. (e) and (f) show line profiles of surface height extracted along $\langle 110 \rangle$ and $\langle 100 \rangle$ directions respectively for the unimplanted and implanted material. Also shown are the surface profiles predicted by CPFE.

The large increase in pile-up in the helium-implanted material can be clearly seen in the surface height profile measured AFM and predicted by CPFE (Figure 3), which agree very well. Line plots were made from AFM and CPFE contour plots in the $\langle 100 \rangle$ and the $\langle 110 \rangle$ directions i.e. direction with minimum and maximum pile-up respectively (Figure 3 (e)-(f)). From the line plots, $\sim 172\%$ increase in pile-up height is seen in the $\langle 110 \rangle$ direction in the implanted sample. A relatively shallower residual indent impression in the implanted sample is consistent with the observed increased hardening in the sample. We note in passing that CPFE uniquely predicts the experimentally observed four-fold pile-up pattern, by constraining slip to the applicable crystallographic slip systems. The contrasting, unphysical uniform distribution of pile-up around the indent, predicted by an isotropic continuum FEM model, is displayed in Figure C.2 (Appendix C) for comparison.

3.2. Residual elastic lattice rotations

Lattice orientation of each point in the sample, represented by rotation matrix \mathbf{R} , was measured by HR-EBSD and Laue diffraction and predicted by CPFE. The average orientation of points in the unimplanted material, far from the indent (22-25 μm and 10 μm below surface for Laue and HR-EBSD respectively) was considered as the orientation of the undeformed material, \mathbf{R}^{ref} . The indentation-induced change in orientation \mathbf{R}^d , for each point with lattice orientation, \mathbf{R} was then calculated as [33]:

$$\mathbf{R} = \mathbf{R}^d \mathbf{R}_{ref} \quad (10)$$

$$\mathbf{R}^d = \mathbf{R} \mathbf{R}_{ref}^{-1} \quad (11)$$

As per the convention adopted in [52], \mathbf{R}^d captures the combined effect of sequential rotation about the X, Y and then Z axis by the lattice rotation angles θ_x , θ_y and θ_z . Provided that $R_{dif\ 31} \neq \pm 1$, the lattice rotation angles were computed for each sample point as [52]:

$$\theta_x = \tan^{-1} \left(\frac{R_{32}^d}{R_{33}^d} \right), \quad \theta_y = -\sin^{-1}(R_{31}^d), \quad \theta_z = \tan^{-1} \left(\frac{R_{21}^d}{R_{11}^d} \right) \quad (12)$$

The lattice rotations in Figure 4 are plotted on virtual YZ slices, at different X positions, for both samples. For HR-EBSD only rotation about the out-of-plane axis θ_x , is considered for one YZ slice through the indent centre. Rotations about the other two axes are not considered as they may have been modified due to stress-relaxation during FIB-lift-out preparation. HR-EBSD and Laue diffraction, respectively have the advantage of high spatial resolution and high angular resolution, and are compared with the CPFÉ predictions using the same colour and length-scales.

The Laue data and CPFÉ predictions of lattice rotations (Figure 4 (a)-(d)) agree reasonably well, particularly for θ_x . Interestingly, agreement is better for slices 5 μm away from the indent centre (positions 1 and 3 in Figure 4 (c)-(d)). The disparity between CPFÉ and Laue data in position 2 is due to the presence of steep strain gradients and rapid variation of lattice rotation at the indent centre. In positions 1 and 3, rotations in the unimplanted sample, particularly θ_x , are significantly larger than in the implanted sample. For quantitative analysis, line plots were extracted, for these two slices, at depths of 4.5 μm from the sample surface, from both Laue and CPFÉ results and superimposed (Figure 5). The line plots distinctly show the surprisingly smaller lattice rotations in the implanted sample, suggesting a more localised deformation.

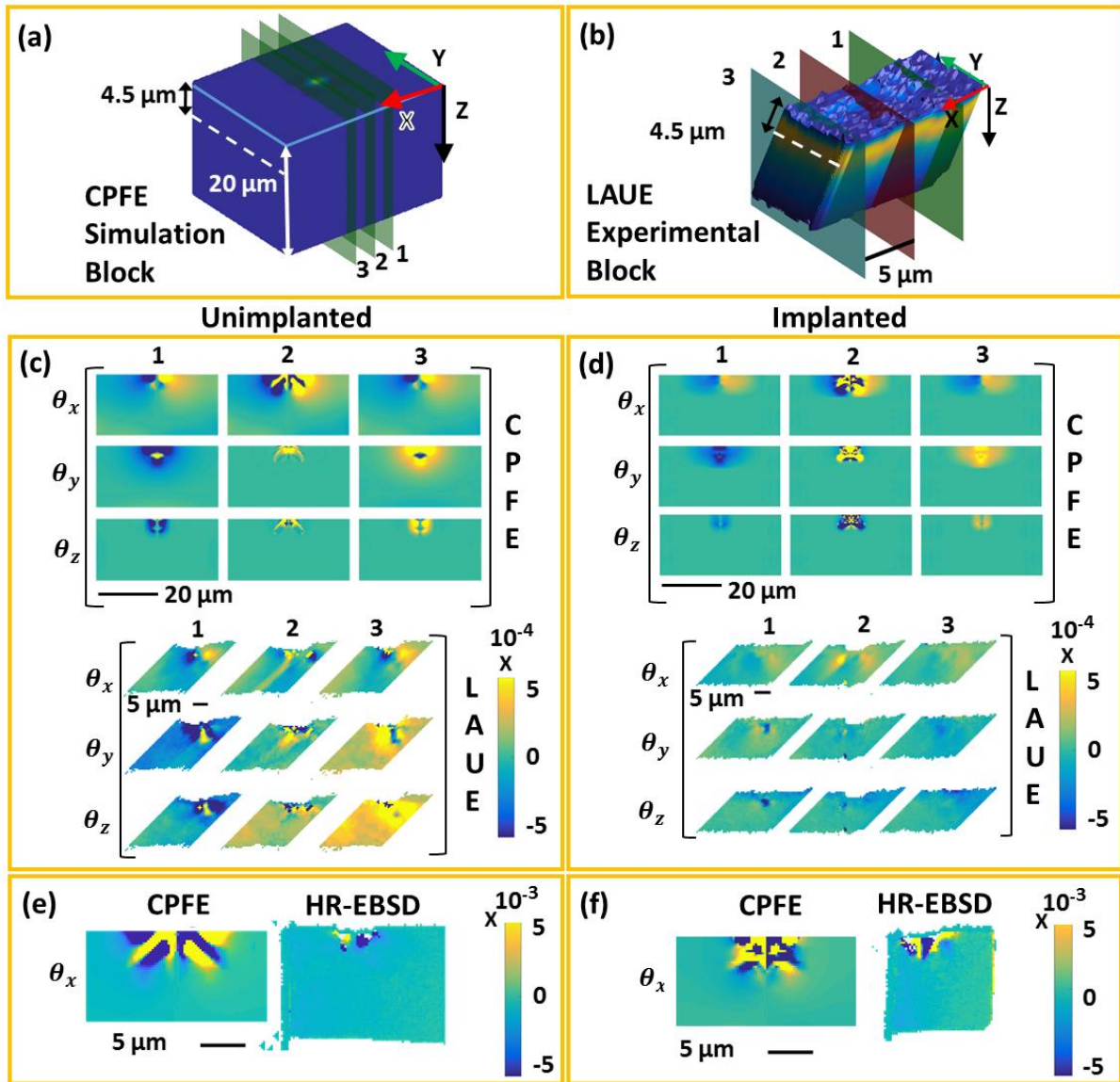


Figure 4 – (a) 3D rendering of the CPFE simulated volume coloured according to the predicted displacement magnitude along the Z axis of the indented tungsten block. X, Y and Z axes are superimposed. Slices 1-3, drawn on the block, represent the three sections along the X-axis (indent centre - slice 2), on which the lattice rotations predicted by CPFE are plotted. (b) Visualization of the sample volume measured by Laue diffraction, coloured according to the experimentally measured intensity. Superimposed are the X, Y, and Z axes, as well as the slices on which the measured lattice rotations are plotted. Comparison of lattice rotations predicted by CPFE and measured by Laue for the (c) unimplanted sample and (d) the helium-implanted sample. Comparison of lattice rotation as predicted by CPFE and measured by HR-EBSD for the (e) unimplanted sample and (f) the helium-implanted sample. With respect to the initial crystallographic coordinates, the X axis points in the $[1 \ -1 \ 0]$ direction, the Y in $[1 \ 1 \ 0]$ direction and the Z in the $[001]$ direction. Data from CPFE simulations and Laue and HR-EBSD experiments are displayed on the same length- and colour-scale. The dotted white lines in (a) and (c) represent the depth at which the line plots in Figure 5 were extracted. Lattice rotations are plotted in radians.

The θ_x line plots from CPFÉ and Laue agree very well in the far field, where small changes in lattice orientation are well captured by the high angular resolution of Laue measurements [25,53,54]. However, in the highly deformed volume below the indent, where steep strain gradients exist, Laue peaks become streaked [55]. This streaking is linked to the underlying GND population within the probed volume, as described, for example by Barabash et al. [56,57]. Unfortunately streaked Laue peaks cannot be fitted as accurately, leading to a loss of strain and lattice rotation resolution in this region. For example, in Figure 4 CPFÉ predicts rapid variations of lattice rotation immediately below the indent that are not resolved by Laue diffraction. The high spatial resolution of HR-EBSD [30,32] complements the Laue measurements by giving detailed information in this region.

Good agreement between HR-EBSD and CPFÉ (Figure 4 (e)-(f)) is seen for both samples in terms of the geometry of the deformation field. However, CPFÉ predicts a slightly wider spread of the rotation field than measured by HR-EBSD. This may be attributed to stress release during FIB-lift-out preparation. Importantly, comparison of CPFÉ and HR-EBSD shows that the magnitude of the rotation field immediately below the indent is similar for both the implanted and unimplanted sample. Thus, the major difference between the implanted and unimplanted material lies in the far-field rotations captured by Laue diffraction.

It is worth noting that using only HR-EBSD or Laue diffraction could lead to incomplete measurement of the deformation field in far-field or near the indent respectively. This underlines the importance of the use of complementary techniques for gaining a complete picture of crystal scale deformation at the nano-scale.

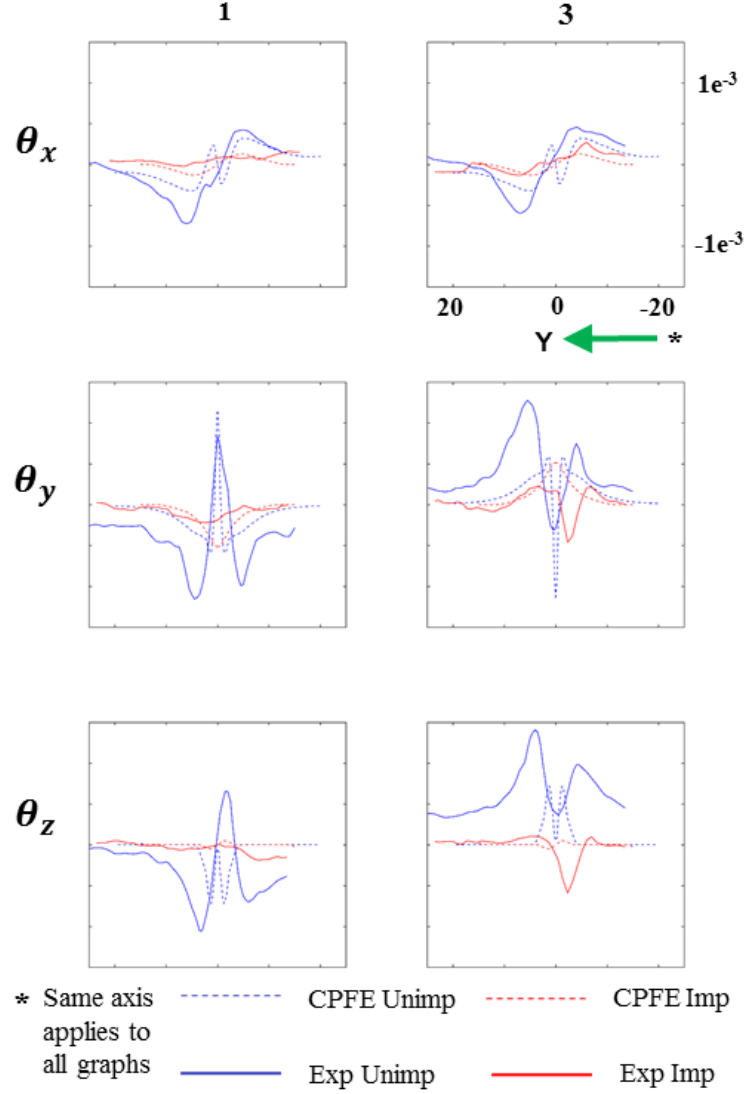


Figure 5 – Line plots corresponding to the contour plots in Figure 4 (c)-(d). Lattice rotations are plotted along a horizontal line 4.5 μm below the indent (line shown by dotted white lines in Figure 4 (a) and (b)). Slices 1 and 3 represent the YZ sections drawn 5 μm away from the indent centre, on either side, along the X-axis in Figure 4 (a) and (b).

3.3. Residual elastic lattice strains

The deviatoric residual lattice strain ($\boldsymbol{\varepsilon}_{dev}^e$) is measured by both Laue diffraction and HR-EBSD. To directly compare the CPFE predictions with the experimental measurements, $\boldsymbol{\varepsilon}_{dev}^e$ is calculated from the total elastic strain tensor ($\boldsymbol{\varepsilon}^e$) given by CPFE:

$$\boldsymbol{\varepsilon}_{dev}^e = \boldsymbol{\varepsilon}^e - \boldsymbol{\varepsilon}_{vol}^e = \boldsymbol{\varepsilon}^e - 1/3 \text{Tr}(\boldsymbol{\varepsilon}^e)\mathbf{I} \quad (13)$$

where $\boldsymbol{\varepsilon}_{vol}^e$ is the volumetric strain. Helium-implantation induces an out-of-plane lattice swelling i.e. positive ε_{zz}^e , while constraints imposed on the implanted layer along X and Y directions (to maintain continuity with the substrate) means that $\varepsilon_{xx}^e = \varepsilon_{yy}^e \approx 0$ [15,42]. As $\text{Tr}(\boldsymbol{\varepsilon}_{dev}^e) = 0$, it may be estimated that, far from the indent in the implanted material, $\varepsilon_{dev_{xx}}^e = \varepsilon_{dev_{yy}}^e = -0.5\varepsilon_{dev_{zz}}^e$. This implantation-induced deviatoric strain is clearly seen in Laue measurements of the implanted sample (Figure 6 (d)); a tensile $\varepsilon_{dev_{zz}}^e$ ($\sim 5.5 \times 10^{-6}$) and compressive $\varepsilon_{dev_{xx}}^e$ and $\varepsilon_{dev_{yy}}^e$ ($\sim -2.5 \times 10^{-6}$) in the implanted layer [10]. It is worth noting that the CPFPE formulation for the implanted sample does not explicitly include the helium-induced lattice swelling. Rather the corrective stress, arising due to restricted deformation in the X and Y directions, is included in the CPFPE model as an additional boundary condition. Consequently the CPFPE predicted strains are purely indentation-induced (direct components of the indentation-induced deviatoric strain referred to as ε_{xx} , ε_{yy} and ε_{zz}). Thus the CPFPE predicted out-of-plane strain for the implanted layer is somewhat smaller than that measured by Laue, where both indentation and implantation induced strains are captured (Figure 6 (d)).

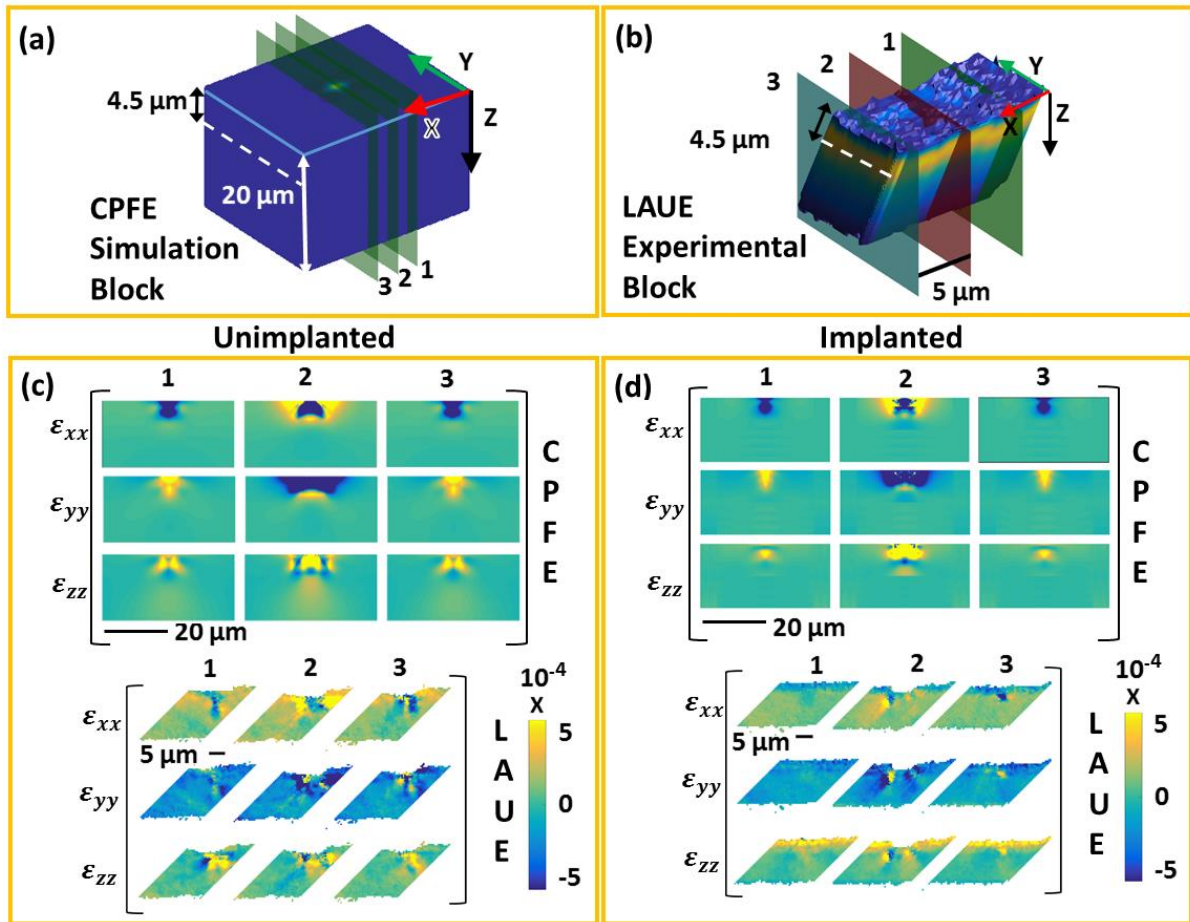


Figure 6 – For the CPFE data: (a) Slices 1-3 drawn on the block represent the three sections along the X-axis (slice 2 being at the indent centre) on which the residual deviatoric elastic strains predicted by CPFE are shown in (c) unimplanted sample and in (d) helium-implanted sample. For the Laue data: (b) Visualisation of the measured sample volume. Superimposed are the X, Y, and Z axes, as well as the slices on which the measured deviatoric elastic lattice strains in (c) the unimplanted sample and (d) the helium-implanted sample are plotted. With respect to the initial crystallographic coordinates, the X axis points in the [1 -1 0] direction, the Y in the [1 1 0] direction and the Z in the [001] direction. Slices 1-3 in experiments and simulations are at the same spatial positions and data in (c) and (d) is displayed on the same length- and colour-scales. The dotted white lines through (a) and (b) represent the depth at which the line plots in Figure D.1 were extracted.

ε_{xx} , ε_{yy} and ε_{zz} , predicted by CPFE and measured by Laue diffraction, are shown in Figure 6, plotted on virtual YZ slices through the sample at different X positions. Good qualitative agreement is observed. Interestingly both the measurements and CPFE predictions show a localisation of indentation induced lattice strain in the implanted sample. Distinctly noticeable is the tightly confined ε_{zz} , at positions 5 μm away from the indent centre (slices 1

and 3 in Figure 6 (d)). The localisation of strain fields is further quantified by line plots drawn for the corresponding contour plots in Figure 6 at depth of 4.5 μm from the sample surface (Appendix D). The agreement between CPFE predictions and experimental measurements inspires some confidence in the CPFE formulation and its foundation hypothesis; localised deformation in slip channels arising from interactions of dislocations with the helium-defects. Importantly, the formulation has a minimal number of fitting parameters; two determined from indentation of the unimplanted material, τ_c^0 and C' , and only one for the helium-implanted material, γ i.e. the softening-rate.

3.4. GND Density

Hardening is implemented in the CPFE formulation as a function of evolving GND densities (Eq. (2)). For the implanted sample, the hardening is accompanied by a strain softening due to removal of helium-implantation-induced defects by glide dislocations (Eq. (3)-(5)). The fine-tuned combination of hardening and softening in the UMAT is vital for the quantitative agreement observed between the CPFE predictions and experimental results for the lattice distortions. The explicit incorporation of GNDs in the formulation is key for introducing length-scale effects as originally proposed by Ashby [58]. Further, the GND distribution can provide insights into the plastic zone size, which can be directly compared to experiments. Following Nye's theory [59], GND densities are thus computed from both HR-EBSD and Laue measurements and compared with the CPFE predictions.

Details of the GND density computation can be found elsewhere [33]. Briefly, the fundamental principle is related to the compatibility of the displacement field, whereby the closure failure induced by plastic deformation, must be balanced by an equal and opposite incompatibility due to elastic deformation. The deformation gradient can be multiplicatively decomposed into the elastic \mathbf{F}^e and plastic component \mathbf{F}^p as described by Lee [35] (further

details in Appendix C). The closure failure, $\langle \mathbf{B} \rangle$, can then be described by either component as

$$\langle \mathbf{B} \rangle = \iint_S (\text{CURL}(\mathbf{F}^p))^T \mathbf{N} dS \cong \iint_S (-\text{CURL}(\mathbf{F}^e))^T \mathbf{N} dS = \iint_S \alpha_{km} N_m dS \quad (14)$$

where, the curl of any second-order tensor V is described by $(\nabla \times V)_{km} = \epsilon_{ijk} V_{mj,i}$ [33].

Nye related $\boldsymbol{\alpha}$ to dislocations inside the crystal. Given q dislocations per unit area with Burgers' vector \mathbf{b} and unit line direction \mathbf{l} threading the plane, with surface unit normal \mathbf{N} , $\boldsymbol{\alpha}$ may be written as

$$\alpha_{km} = q b_k l_m \quad (15)$$

Defining $\rho_m = q l_m$ means $\alpha_{km} = b_k \rho_m$. So $\boldsymbol{\alpha}$ for a general slip system λ may be written as

$$\boldsymbol{\alpha} = \sum_{\lambda} (\mathbf{b}^{\lambda} \otimes \boldsymbol{\rho}^{\lambda}) \quad (16)$$

As \mathbf{F}^e arises from lattice rotation and strain, $\boldsymbol{\alpha}$ can be computed as $\boldsymbol{\alpha} \cong (-\text{curl}(\boldsymbol{\epsilon}^e + \boldsymbol{\omega}^e))^T$. Reshaping the 3×3 $\boldsymbol{\alpha}$ tensor as a 9×1 column vector and representing densities of j dislocation types as a column vector $\boldsymbol{\rho}$, Eq. (16) can be re-written as

$$\mathbf{A}\boldsymbol{\rho} = \boldsymbol{\alpha} \quad (17)$$

where \mathbf{A} is a linear operator ($9 \times j$ matrix, for j types of dislocations), where the j^{th} column contains the dyadic product of the Burgers' vector and line direction of the j^{th} dislocation type. Since generally $j > 9$ there is no unique solution for $\boldsymbol{\rho}$. Instead, knowing $\boldsymbol{\alpha}$ and \mathbf{A} , optimization methods may be used to obtain $\boldsymbol{\rho}$. Here, the GND density $\boldsymbol{\rho}$ was computed using the L2 optimisation technique [60], which minimizes the sum of squares of dislocation densities i.e. $\sum_j \rho_j^2 = \boldsymbol{\rho}^T \cdot \boldsymbol{\rho}$. Previous work showed that L2, while mathematically simple, can reliably predict the sum of GND densities over all slip systems [33].

We assume, consistent with the CPFE calculations, that deformation in bcc tungsten is accommodated by dislocations with $a/2\langle 111 \rangle$ Burgers vector gliding on $\{110\}$ planes

[61,62] (a list of Burgers vector and line directions considered is provided in Appendix E). Furthermore, we assume dislocations to be of either pure edge or pure screw type, resulting in 16 dislocation types in total (four screw types with $\langle 111 \rangle$ line directions and twelve edge types with $\langle 112 \rangle$ line directions; Table E.1).

Figure 7 shows the total GND density computed from HR-EBSD, Laue diffraction and CPFÉ datasets, plotted on the YZ, XZ and the XY cross sections at the indent centre. To enable a direct comparison with both Laue and HR-EBSD measurements, the CPFÉ predictions are plotted on two different length scales. Complementing each other, the high angular resolution of Laue measurements [25,26] and high spatial resolution of HR-EBSD measurements [30,63] detect the far-field and near-field deformation respectively. In the unimplanted sample, a small zone of high GND density is seen close to the indent (Figure 7 (d)), with a surrounding large zone of low GND density (Figure 7 (c)). In contrast the implanted sample shows a relatively larger zone of high GND density surrounding the indent (Figure 7 (h)), with a surprisingly sharp boundary and very low GND density outside this region (Figure 7 (g)). The experimental observations show a similar picture, consistent with the predictions from CPFÉ.

The CPFÉ formulation for the helium-implanted sample was based on the hypothesis of removal of helium-implantation-induced obstacles by the progressive passage of dislocations. This leads to defect-free slip channels that accommodate deformation in the implanted zone, near the indent, and give rise to a large pile up. As a result a more compact plastic zone is expected in the implanted material, which is clearly seen in the spatial variation of GND density predicted by CPFÉ and observed in experiments.

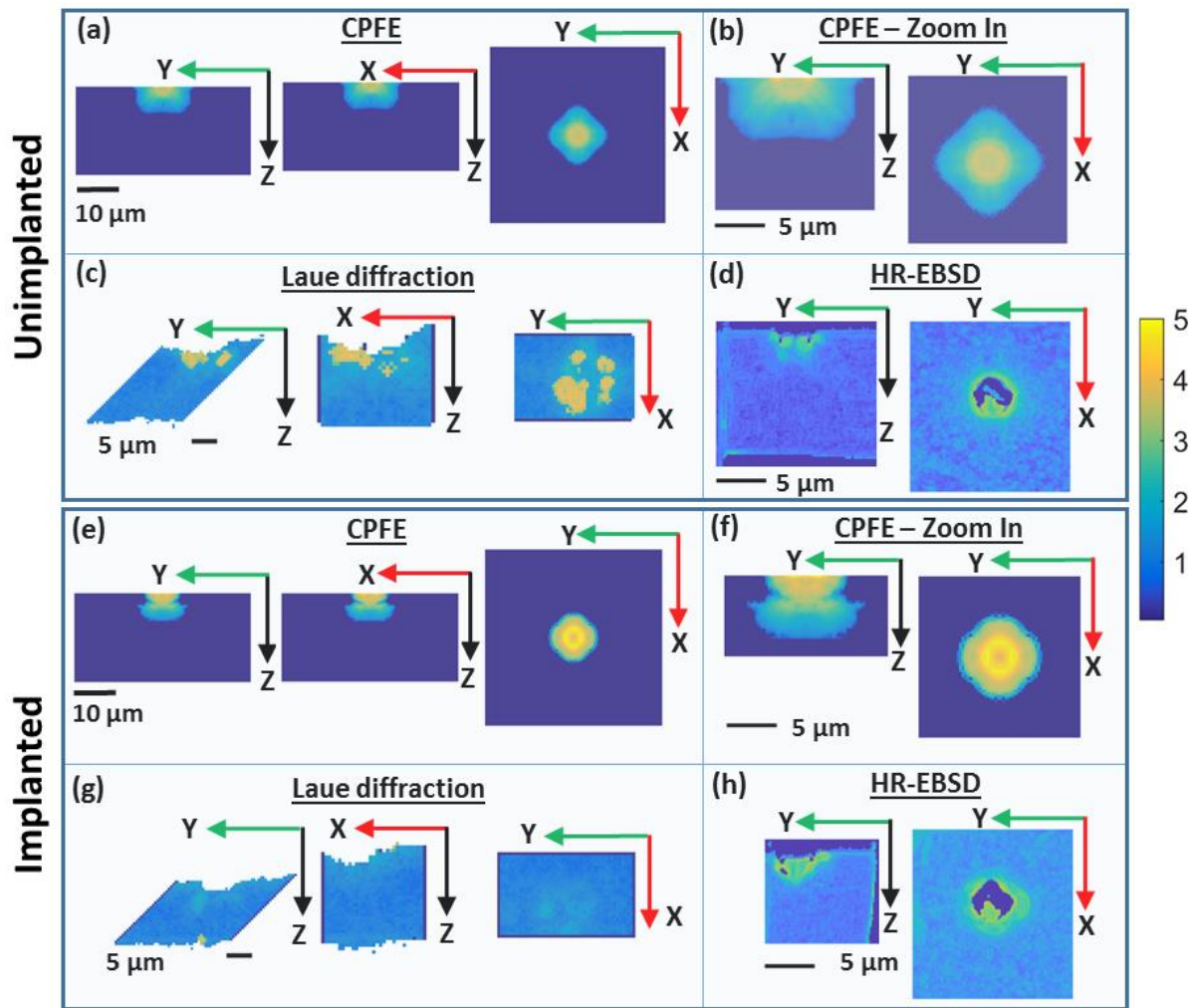


Figure 7 – Total GND density plotted on YZ, XZ and the XY cross-sections through the indent centre. GND was calculated using L2 optimisation. Predictions from CPFE calculations are shown in (a) and (b) for the unimplanted sample, and (e) and (f) for the helium-implanted sample. GND density computed from Laue diffraction measurements for the unimplanted and implanted samples are shown in (c) and (g) respectively. GND density determined by HR-EBSD for the unimplanted and the implanted sample is shown in (d) and (h) respectively. The same colour scale is used for all plots showing $\log_{10}(\rho)$ with ρ in $1/\mu\text{m}^2$. (a), (c), (e) and (f) are plotted on the same length scale. (b), (d), (f) and (h) show magnified plots of GND density and are also all shown on the same length scale.

An important point to note from Figure 7 is the size of the plastic zone surrounding each indent. The results show that, although the indent is only 500 nm deep, the affected zone extends beyond the $\sim 3 \mu\text{m}$ thick implanted layer. This implies that the underlying substrate can have a significant impact on the results, even when the indentation depth is $< 20\%$ of the implanted layer thickness. Generally, when nano-indentation is performed on thin film on

substrates, the contribution of the underlying substrate is carefully accounted for [64–66]. However, in most studies investigating indentation response of irradiated materials, indentation depth of $\sim 20\%$ of the implanted layer thickness is used and the effect of the underlying substrate is not considered explicitly [67–69]. Our result highlights that to ensure fidelity it is important to account for the combined effect of the implanted layer and the substrate. An analysis whereby the implanted layer is approximated as an infinite half space may render inaccurate result.

4. Conclusion

We have presented a comprehensive experimental and modelling study of the effect of helium-implantation damage on the mechanical properties of tungsten. TEM of the cross-section of an indent in the implanted sample showed that dislocations “sweep out” helium-implantation-induced defects, leaving behind low defect density zones/channels. This “sweeping out” leads to a localisation of deformation and a softening of the material with increasing plastic deformation. Qualitatively this explains the substantial increase in pile-up and the localisation of deformation leading to slip steps. A physically-based CPFEM model was constructed where initial hardening due to interaction of dislocation with irradiation defects, as well as subsequent softening is accounted for. Importantly this model only has three free parameters, of which only one is fitted to the implanted material. It successfully captures the changes in load-displacement curve, changes in pile-up structure, lattice rotations and residual lattice strains, as well as GND population in remarkably good agreement with our experimental observations. The results highlight that even a comparatively small concentration of irradiation/implantation induces defects – 1500 appm – can bring about dramatic changes in the mechanical behaviour, with strain hardening being replaced by a large increase in the initial hardness followed by strain softening. Understanding these changes in detail and having physically-based models that capture these effects will be key

for determining the evolution of properties in fusion reactor armour components and assessing their in-service performance.

Acknowledgements

We thank N. Peng for performing the ion-implantation, M. Rieth for providing the tungsten single crystal sample, R. Xu and W. Liu for their help with X-ray diffraction experiments, A. London and D. Nguyen-Manh for their insightful comments, and A.J. Wilkinson for providing the software for HR-EBSD analysis. This work was funded by Leverhulme Trust Research Project Grant RPG-2016-190, and used resources of the Advanced Photon Source, a U.S. Department of Energy (DOE) Office of Science User Facility operated for the DOE Office of Science by Argonne National Laboratory under Contract No. DE-AC02-06CH11357. Ion implantations were performed under the UK Engineering and Physical Sciences Research Council grant EP/H018921/1. ET acknowledges financial support from the Engineering and Physical Sciences Research Council Fellowship grant EP/N007239/1. Electron and atomic force microscopy were performed at the David Cockayne Centre for Electron Microscopy, Department of Materials, and at the LIMA lab, Department of Engineering Science, both at the University of Oxford.

Appendix A

List of 13 ion energies used and the corresponding fluence for the helium ion implantations:

Ion Energy (MeV)	3000 appm He
	Fluence (ions/cm ²)
0.05	2.40E+15
0.1	1.80E+15
0.2	4.20E+15
0.3	1.20E+15
0.4	4.80E+15
0.6	5.20E+15
0.8	5.00E+15
1	5.00E+15
1.2	5.00E+15
1.4	5.00E+15
1.6	5.50E+15
1.8	7.00E+15
2.0	5.00E+15

Table A.1 - List of 13 ion energies used and the corresponding fluences for the helium ion implantations.

Appendix B

The stiffness of tungsten (material for the sample block) is a significant fraction (~36%) of that of diamond (material for the indenter tip) (Table B.1). However simulations using a rigid sharp indenter showed that the simulation results matched the experimental results very well when the results were scaled using the effective modulus, E_{eff} [34]

$$P (exp.) = \frac{E_{eff} (exp.)}{E (FEA)} P(FEA) \quad (B.1)$$

Thus, to avoid a full meshing and increase in simulation size, the indenter was designed as a discrete rigid wire frame.

$E_{diamond}$	$E_{tungsten}$	$\nu_{diamond}$	$\nu_{tungsten}$	E_{eff}	$R_{indenter}$
1143 GPa	410 GPa	0.0691	0.28	322.58 GPa	4.2 μm

Table B.1 – Values of Young's modulus and Poisson's ratio for diamond (indenter tip) and tungsten (indented sample) as obtained from literature [70–72]².

P (exp.) Unimplanted	Targeted - P (FEA) Simulated	P (exp.) Implanted	Targeted - P (FEA) Simulated
48.8 mN	61.4 mN	82.5 mN	104.88 mN

Table B.2 – Scaling of the load values from experiment to Finite element simulation, using the $E_{eff} = 322.58$ GPa and $E_{tungsten} = 410$ GPa

Simulations were carried out to reproduce the experimental results i.e. the load displacement curves obtained through nano-indentation and the height profile around the indent measured by AFM. The parameters in the UMAT were adjusted to match the targeted load values as in Table B.2. The targeted load values were calculated using Eq. (B.1) with $E_{eff} = 322.58$ GPa and $E_{tungsten} = 410$ GPa, to account for the elastic properties of the diamond indenter tip [34].

² With the assumption of isotropic, linear elastic solid, the Young's modulus and Poisson's ratio are related to the elastic constant as follows: $E = c_{11} - 2 \left(\frac{c_{12}^2}{c_{11} + c_{12}} \right)$ and $\nu = c_{12} / (c_{11} + c_{12})$.

The simulated load was then scaled back with respect to E_{eff} (to match the experimental results) for ease of comparison with the experimental results.

Appendix C

In the 3D CPFEM model a constitutive law incorporating crystallographic slip was used to predict the mechanical response of the tungsten BCC crystal under indentation. Each time the UMAT is called by Abaqus, it is provided with the deformation gradient (\mathbf{F}) at the beginning and end of the time increment and the internal state variables at the beginning of the time increment. Using the material properties and constitutive law, the UMAT implicitly computes and returns to Abaqus the updated values of the state variables at the end of the time increment, the updated stress state ($\boldsymbol{\sigma}_{t+\Delta t}$) and the material Jacobian ($\frac{\partial \Delta \boldsymbol{\sigma}}{\partial \Delta \boldsymbol{\varepsilon}}$). Details pertaining to how the deformation gradient provided by Abaqus is used by the UMAT to solve the incremental plastic strain and to update the stress state can be found elsewhere [33].

The framework of crystal plasticity being used here is based on the well-established method of decomposing the deformation gradient (\mathbf{F}) into elastic and plastic tensors [33,35]

$$\mathbf{F} = \frac{\partial \mathbf{x}}{\partial \mathbf{X}} = \mathbf{F}^e \mathbf{F}^p \quad (\text{C.1})$$

\mathbf{F}^p can be defined in terms of the crystallographic slip $\boldsymbol{\beta}^p$ (relative displacement of two slip planes separated by a unit distance), slip direction \mathbf{s} and slip plane normal \mathbf{n} . The crystallographic plane normals and the slip directions are updated as the crystal lattice undergoes deformation. For a finite number of slip systems, \mathbf{F}^p is given by

$$\mathbf{F}^p = \mathbf{I} + \frac{\partial \mathbf{u}^p}{\partial \mathbf{X}} = \mathbf{I} + \boldsymbol{\beta}^p = \mathbf{I} + \sum_{\lambda} \beta^{p\lambda} (\mathbf{s}^{\lambda} \otimes \mathbf{n}^{\lambda}) \quad (\text{C.2})$$

The rate of change of \mathbf{F}^p is thus

$$\dot{\mathbf{F}}^p = \sum_{\lambda} \dot{\beta}^{p\lambda} (\mathbf{s}^{\lambda} \otimes \mathbf{n}^{\lambda}) \quad (\text{C.3})$$

where $\dot{\beta}^{p\lambda}$ is the crystallographic slip rate on slip system λ . The velocity gradient \mathbf{L} is given by $\dot{\mathbf{F}}\mathbf{F}^{-1}$. \mathbf{L} can be split into symmetric and anti-symmetric components to give the rate of deformation \mathbf{D} and the continuum spin \mathbf{W} respectively. \mathbf{D} can be written as

$$\mathbf{D} = \mathbf{D}^e + \text{sym}(\mathbf{F}^e \mathbf{L}^p \mathbf{F}^{e-1}) \cong \mathbf{D}^e + \text{sym}(\mathbf{L}^p) \cong \mathbf{D}^e + \mathbf{D}^p \quad (\text{C.4})$$

\mathbf{D}^e is computed using Hooke's law, while \mathbf{D}^p is approximated by the symmetric part of \mathbf{L}^p . For small deformations, \mathbf{L}^p is approximated as equal to $\dot{\mathbf{F}}^p$ i.e. Eq. (C.3). \mathbf{D}^p approximated from \mathbf{L}^p gives the increment in the plastic strain ($\Delta\boldsymbol{\varepsilon}_p = \mathbf{D}^p \Delta t$), while the elastic rotation is calculated from the asymmetric component of \mathbf{L}^e where

$$\mathbf{L}^e = \mathbf{L} - \mathbf{F}^e \mathbf{L}^p \mathbf{F}^{e-1} \quad (\text{C.5})$$

Material Property	Value	Reference
Elastic modulus E	410 GPa	[70–73]
Shear modulus G	164.4 GPa	[70–73]
Poisson's ratio ν	0.28	[70–73]
Burgers' vector b	2.7×10^{-10} m	[74]
τ_H^0	750 MPa	Section 2.6.1 & C.1
Helmholtz free energy ΔF	0.85 eV	Section C.2
Boltzmann constant k	1.381×10^{-23} J/K	[75]
Temperature T	298 K	Room temperature assumed similar to experimental conditions
Stress boundary conditions $\sigma_{xx}^{BC} = \sigma_{yy}^{BC}$	-262.704 MPa	Section C.3
Attempt frequency ν	1×10^{19} s ⁻¹	[76]
Density of statistically stored dislocations, ρ_{SSD}	1×10^{10} m ⁻²	Section C.4
Density of mobile dislocations ρ_m	1.75×10^{13} m ⁻²	Section C.4
Probability of pinning Ψ	0.657×10^{-2}	Value chosen and kept fixed
τ_c^0	360 MPa	Fitted to experimental data of unimplanted sample
γ	0.025	Fitted to experimental data of helium-implanted sample
C'	0.0065	Fitted to experimental data of unimplanted sample

Table C.1– List of parameters used in the constitutive law in the CPFE formulation and their corresponding values.

Section C.1: Determination of the value of τ_H^0

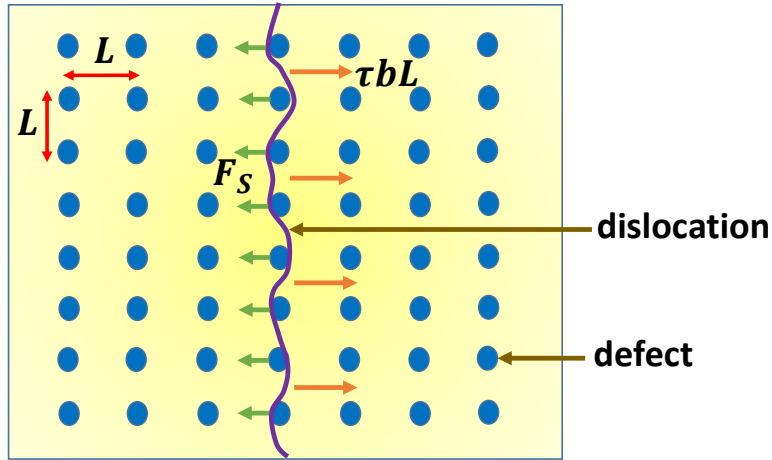


Figure C.1 – View of the slip plane interspersed with helium-implantation induced defects with a dislocation line trying to pass through.

Section C.2: Determination of the value of ΔF

ΔF is the differential free energy arising from the nucleation of an embryonic kink pair (one with minimum lattice separation) [77]. This can be defined in terms of kink-pair enthalpy ΔH , the entropy ΔS and the temperature T

$$\Delta F = \Delta H - T\Delta S \quad (C.6)$$

At the simulation temperature screw dislocations experience higher lattice friction and thus lower mobility than edge dislocations. Thus the rate controlling mechanism is governed by the screw dislocation mobility [78]. Thus, we use the kink-pair nucleation enthalpy (ΔH) corresponding to screw dislocation mobility as the governing factor for computing ΔF .

The kink-pair enthalpy ΔH is a function of the applied stress and tends to zero when the applied stress nears the Peierls stress τ_p [77]. Given the applied stress (τ) and Peierls stress, ΔH can be written as

$$\Delta H = \Delta H_0 \left(1 - \left(\frac{\tau}{\tau_p} \right)^p \right)^q \quad (\text{C.7})$$

Thus ΔF can be re-written as

$$\Delta F = \Delta H_0 \left(1 - \left(\frac{\tau}{\tau_p} \right)^p \right)^q - T\Delta S \quad (\text{C.8})$$

For tungsten ΔH_0 is 1.63 eV, p is 0.86, q is 1.69 [79] and $\tau_p \sim 1640$ MPa (as computed from the Peierls barrier using DFT [80]). The standard entropy of solid tungsten is 32.66 J/(mol K) [81], which is $\Delta S \sim 4k$ where k is the Boltzmann's constant (1.38×10^{-23} J/K) and the temperature is $T = 298$ K (as per the experimental conditions). ΔF is computed by choosing a value for the applied stress τ to be equal to the initial value of critically resolved shear stress (CRSS) $\tau_c^0 = 360$ MPa = $0.22\tau_p$ (as obtained by fitting to the experimental data) and is kept fixed throughout the simulation. The effect of the changing CRSS (with hardening due to GNDs), the changing applied stress field (τ) with progressive deformation and the work done by the changing differential stress field ($|\tau| - \tau_c$) is accounted for in the $\sinh(\)$ part of the slip law.

The value of ΔF is thus computed to be 0.85 eV or 1.36×10^{-19} J. This is in the range of the estimated order of magnitude of ΔF for self-diffusion at room temperature i.e. 10^{-19} J/atom and 10^{-21} J/atom [76]. A high value of ΔF as computed in this case ensures that the rate sensitivity will be controlled by the hardening law for the evolution of slip resistance and not the thermal activation energy.

Section C.3: Determination of the value of σ_{xx}^{BC} and σ_{yy}^{BC}

The ε_{zz}^{dev} component of the deviatoric lattice strain in the helium-implanted sample, as measured by the white-beam Laue diffraction experiment is $\sim 550 \times 10^{-6}$. This value was obtained by averaging the measured ε_{zz}^{dev} over 1.5 μm of the helium-implanted layer. The ε_{zz}

component of the total strain tensor was then computed from ε_{zz}^{dev} . The total strain tensor, $\boldsymbol{\varepsilon}^e$, is related to the deviatoric component $\boldsymbol{\varepsilon}_{dev}^e$ as

$$\boldsymbol{\varepsilon}^e = \boldsymbol{\varepsilon}_{dev}^e + 1/3 \text{Tr}(\boldsymbol{\varepsilon}^e)\mathbf{I} \quad (\text{C.9})$$

where \mathbf{I} is the identity matrix. The ε_{xx} and ε_{yy} components of the total lattice strain tensor are expected to be zero, as deformation along X and Y directions is restricted in order to maintain geometrical continuity between the implanted layer and the substrate [42]. Thus $\text{Tr}(\boldsymbol{\varepsilon}^e) = \varepsilon_{zz}$. Therefore, Eq. (C.9) can be re-written as

$$\varepsilon_{zz} = \varepsilon_{zz}^{dev} + 1/3 \varepsilon_{zz} \quad (\text{C.10})$$

$$\varepsilon_{zz}^{dev} = 2/3 \varepsilon_{zz} \quad (\text{C.11})$$

Using Eq. (C.11), $\varepsilon_{zz} = 825 \times 10^{-6}$.

The measured total out-of-plane lattice strain, ε_{zz} is a combination of two components; the defect induced Eigenstrain component (induced strain if the implanted layer were subject to traction-free boundary conditions) and a second component, due to Poisson's effect arising owing to the constraint imposed on the implanted layer along the in-plane directions. Since tungsten is almost elastically isotropic at room temperature [70,71], ε_{zz} can be used to estimate the underlying Eigenstrain by accounting for the lateral constraints on the implanted layer using a correctional strain tensor term ε_{corr} . Here we assume a random orientation of defects giving rise to a pure volumetric Eigenstrain ε_{vol}^* , instead of considering a more complex Eigenstrain with non-zero deviatoric component [82]. In this regime of small strain, the total lattice strain ε_{lat} may be additively decomposed as

$$\varepsilon_{lat} = \varepsilon_{vol}^* + \varepsilon_{corr} \quad (\text{C.12})$$

The volumetric Eigenstrain tensor ε_{vol}^* , is given by $\begin{bmatrix} \varepsilon_{vol}^*/3 & 0 & 0 \\ 0 & \varepsilon_{vol}^*/3 & 0 \\ 0 & 0 & \varepsilon_{vol}^*/3 \end{bmatrix}$. Accounting

for lateral constrains on the implanted layer, we assume $\varepsilon_{xx} = \varepsilon_{yy} \approx 0$. Thus, $\varepsilon_{corr_{xx}} = \varepsilon_{corr_{yy}} = -\varepsilon_{vol}^*/3$. Considering Poisson's effect

$$\varepsilon_{corr_{xx}} = -\frac{\varepsilon_{vol}^*}{3} = \frac{1}{E}(\sigma_{corr_{xx}} - \nu(\sigma_{corr_{yy}} + \sigma_{corr_{zz}})) \quad (C.13)$$

where, E is the elastic modulus and ν the Poisson's ratio. $\sigma_{corr_{zz}} = 0$ as there is no boundary condition in the Z direction and $\sigma_{corr_{xx}}$ is considered equal to $\sigma_{corr_{yy}}$, owing to symmetry.

Thus,

$$\varepsilon_{corr_{xx}} = -\frac{\varepsilon_{vol}^*}{3} = \frac{1}{E}(\sigma_{corr_{xx}} - \nu(\sigma_{corr_{yy}} + \sigma_{corr_{zz}})) = \frac{\sigma_{corr_{xx}}}{E} (1 - \nu) \quad (C.14)$$

Rearranging we get,

$$\sigma_{corr_{xx}} = \frac{-E\varepsilon_{vol}^*}{3(1-\nu)} = \sigma_{corr_{yy}} \quad (C.15)$$

Now $\varepsilon_{corr_{zz}}$, may be written in terms of $\sigma_{corr_{xx}}$ and $\sigma_{corr_{yy}}$

$$\varepsilon_{corr_{zz}} = \frac{1}{E} \left(\sigma_{corr_{zz}} - \nu(\sigma_{corr_{xx}} + \sigma_{corr_{yy}}) \right) = \frac{2\varepsilon_{vol}^*\nu}{3(1-\nu)} \quad (C.16)$$

As per Eq. (C.12), $\varepsilon_{lat_{33}} = \varepsilon_{vol_{33}}^* + \varepsilon_{corr_{33}}$ i.e.

$$\varepsilon_{zz} = \frac{\varepsilon_{vol}^*}{3} + 2 \left(\frac{\nu}{1-\nu} \right) \left(\frac{\varepsilon_{vol}^*}{3} \right) \quad (C.17)$$

We note here, that the volumetric strain component of ε_{lat} , i.e. ε_{vol} is given by $(\varepsilon_{xx} + \varepsilon_{yy} + \varepsilon_{zz})$ and is different from the volumetric Eigenstrain ε_{vol}^* . $\varepsilon_{vol} = \varepsilon_{zz}$ (as $\varepsilon_{xx} = \varepsilon_{yy} \approx 0$), would be equal to ε_{vol}^* , if $\nu = 0.5$. This does not apply for tungsten with $\nu = 0.28$.

Knowing, ε_{zz} , ε_{vol}^* is computed to be 1.4×10^{-3} from Eq. (C.17). Substituting this value in Eq. (C.15), the stress boundary conditions, $\sigma_{corr_{xx}} = \sigma_{corr_{yy}}$ are computed to be -260 MPa.

Section C.4: Estimating values for SSD

Laue diffraction measurements performed on nano-indented pure tungsten showed the presence of GND density on the order of $\sim 10^{18} \text{ m}^{-2}$. This value agreed well with CPFEM predictions of the indentation experiment [33]. The SSD densities assumed here, ρ_{SSD} and ρ_m , for the CPFEM calculations were taken to be much smaller than the GND density estimate, on the order of $10^{10} - 10^{13} \text{ m}^{-2}$.

Section C.5: Comparison of CPFEM with Continuum-mode FEM

The surface pile-up around the nano-indent in the helium-implanted material was predicted quite accurately as seen in Figure 3 where CPFEM prediction and AFM measurements are compared. CPFEM uniquely allows the prediction of the deformation pattern by accounting for crystallographic slip. A continuum plasticity simulation, performed on the same model, is unable to reproduce the orientation dependence of pile-up as shown in Figure C.2.

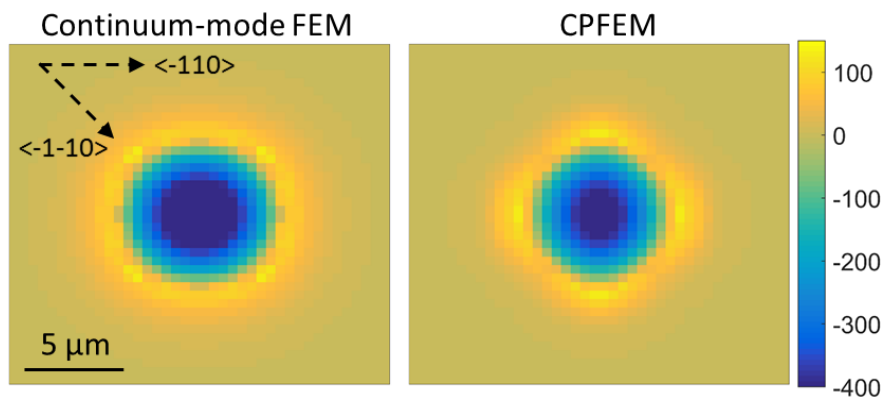


Figure C.2 – Surface pile-up around nano-indentations in 001-oriented helium-implanted tungsten single crystal as predicted by continuum-based simulation (left) and by CPFEM (right).

Appendix D

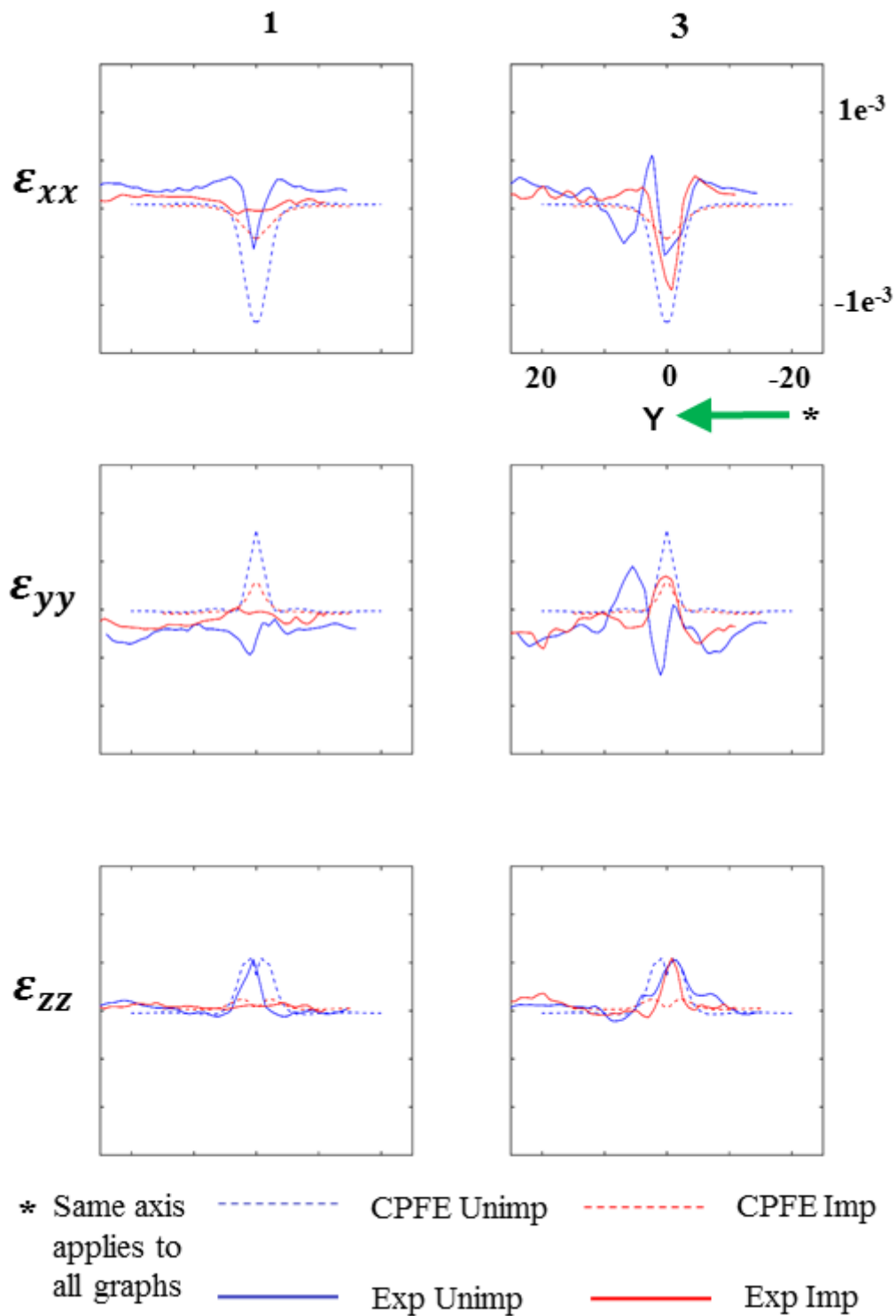


Figure D.1 - Line plots corresponding to the contour plots in Figure 6 (c) and (d). Direct lattice strains are plotted along a horizontal line 4.5 μm below the indent (shown by dotted white lines in Figure 6 (a) and (b)). Slices 1 and 3 correspond to YZ sections drawn 5 μm away from the indent centre, on either side, along the X-axis.

Appendix E

Table E.1 shows the combination of Burgers' vector and line direction used for GND density calculation.

Dislocation type	Density	Burgers' vector : \mathbf{b}	Slip Normal : \mathbf{n}	Line Direction : \mathbf{l}
Edge 1	ρ_1	[-111]	(110)	[-1 1 -2]
Edge 2	ρ_2	[1-11]	(110)	[-1 1 2]
Edge 3	ρ_3	[111]	(-101)	[1 -2 1]
Edge 4	ρ_4	[1-11]	(-101)	[-1 -2 -1]
Edge 5	ρ_5	[111]	(-110)	[-1 -1 2]
Edge 6	ρ_6	[11-1]	(-110)	[1 1 2]
Edge 7	ρ_7	[111]	(01-1)	[-2 1 1]
Edge 8	ρ_8	[-111]	(01-1)	[-2 -1 -1]
Edge 9	ρ_9	[1-11]	(011)	[-2 -1 1]
Edge 10	ρ_{10}	[11-1]	(011)	[2 -1 1]
Edge 11	ρ_{11}	[-111]	(101)	[1 2 -1]
Edge 12	ρ_{12}	[11-1]	(101)	[1 -2 -1]
Screw 1	ρ_{13}	[-111]	(110)	[-1 1 1]
Screw 2	ρ_{14}	[1-11]	(110)	[1 -1 1]
Screw 3	ρ_{15}	[111]	(-101)	[1 1 1]
Screw 4	ρ_{16}	[11-1]	(-110)	[1 1 -1]

Table E.1 - Combination of Burgers' vector and line direction used for the calculation of the GND

REFERENCES

- [1] M. Ekman, K. Persson, G. Grimvall, Phase diagram and lattice instability in tungsten \pm rhenium alloys, *J. Nucl. Mater.* 278 (2000) 276–279. doi:[https://doi.org/10.1016/S0022-3115\(99\)00241-X](https://doi.org/10.1016/S0022-3115(99)00241-X).
- [2] N. Wei, T. Jia, X. Zhang, T. Liu, Z. Zeng, X. Yang, First-principles study of the phase stability and the mechanical properties of W-Ta and W-Re alloys, *AIP Adv.* 4 (2014) 57103. doi:[10.1063/1.4875024](https://doi.org/10.1063/1.4875024).
- [3] M. Rieth, S.L. Dudarev, S.M. Gonzalez de Vicente, J. Aktaa, T. Ahlgren, S. Antusch, D.E.J. Armstrong, M. Balden, N. Baluc, M.-F. Barthe, W.W. Basuki, M. Battabyal, C.S. Becquart, D. Blagoeva, H. Boldyryeva, J. Brinkmann, M. Celino, L. Ciupinski, J.B. Correia, A. De Backer, C. Domain, E. Gaganidze, C. García-Rosales, J. Gibson, M.R. Gilbert, S. Giusepponi, B. Gludovatz, H. Greuner, K. Heinola, T. Höschen, A. Hoffmann, N. Holstein, F. Koch, W. Krauss, H. Li, S. Lindig, J. Linke, C. Linsmeier, P. López-Ruiz, H. Maier, J. Matejcek, T.P. Mishra, M. Muhammed, A. Muñoz, M. Muzyk, K. Nordlund, D. Nguyen-Manh, J. Opschoor, N. Ordás, T. Palacios, G. Pintsuk, R. Pippan, J. Reiser, J. Riesch, S.G. Roberts, L. Romaner, M. Rosiński, M. Sanchez, W. Schulmeyer, H. Traxler, A. Ureña, J.G. van der Laan, L. Veleva, S. Wahlberg, M. Walter, T. Weber, T. Weitkamp, S. Wurster, M.A. Yar, J.H. You, A. Zivelonghi, Recent progress in research on tungsten materials for nuclear fusion applications in Europe, *J. Nucl. Mater.* 432 (2013) 482–500. doi:[10.1016/j.jnucmat.2012.08.018](https://doi.org/10.1016/j.jnucmat.2012.08.018).
- [4] M.R. Gilbert, S.L. Dudarev, S. Zheng, L.W. Packer, J.-C. Sublet, M.R.G. and S.L.D. and S.Z. and L.W.P. and J.-C. Sublet, M.R. Gilbert, S.L. Dudarev, S. Zheng, L.W. Packer, J.-C. Sublet, An integrated model for materials in a fusion power plant: transmutation, gas production, and helium embrittlement under neutron irradiation, *Nucl. Fusion.* 52 (2012) 83019. doi:[10.1088/0029-5515/52/8/083019](https://doi.org/10.1088/0029-5515/52/8/083019).
- [5] C.S. Becquart, M.F. Barthe, A. De Backer, Modelling radiation damage and He production in tungsten, *Phys. Scr.* T145 (2011) 14048. doi:[10.1088/0031-8949/2011/T145/014048](https://doi.org/10.1088/0031-8949/2011/T145/014048).
- [6] C.S. Becquart, C. Domain, An object Kinetic Monte Carlo Simulation of the dynamics of helium and point defects in tungsten, *J. Nucl. Mater.* 385 (2009) 223–227. doi:[10.1016/j.jnucmat.2008.11.027](https://doi.org/10.1016/j.jnucmat.2008.11.027).
- [7] D.E.J. Armstrong, P.D. Edmondson, S.G. Roberts, Effects of sequential tungsten and helium ion implantation on nano-indentation hardness of tungsten, *Appl. Phys. Lett.* 251901 (2013) 1–5. doi:[10.1063/1.4811825](https://doi.org/10.1063/1.4811825).
- [8] F. Hofmann, D.R. Mason, J.K. Eliason, A.A. Maznev, K.A. Nelson, S.L. Dudarev, Non-Contact Measurement of Thermal Diffusivity in Ion-Implanted Nuclear Materials, *Sci. Rep.* 5 (2015) 16042. doi:[10.1038/srep16042](https://doi.org/10.1038/srep16042).
- [9] C.E. Beck, F. Hofmann, J.K. Eliason, A.A. Maznev, K.A. Nelson, D.E.J. Armstrong, D.E.J. Armstrong, Correcting for contact area changes in nanoindentation using surface acoustic waves, *Scr. Mater.* 128 (2017) 83–86. doi:[10.1016/j.scriptamat.2016.09.037](https://doi.org/10.1016/j.scriptamat.2016.09.037).
- [10] S. Das, D.E.J. Armstrong, Y. Zayachuk, W. Liu, R. Xu, F. Hofmann, The effect of helium implantation on the deformation behaviour of tungsten: X-ray micro-diffraction and nanoindentation, *Scr. Mater.* 146 (2018) 335–339. doi:[10.1016/j.scriptamat.2017.12.014](https://doi.org/10.1016/j.scriptamat.2017.12.014).
- [11] Z. Zhou, M.L. Jenkins, S.L. Dudarev, A.P. Sutton, M.A. Kirk, Simulations of weak-beam diffraction contrast images of dislocation loops by the many-beam Howie-Basinski equations, 2006. doi:[10.1080/14786430600615041](https://doi.org/10.1080/14786430600615041).
- [12] D.E.J. Armstrong, A.J. Wilkinson, S.G. Roberts, Mechanical properties of ion-implanted tungsten–5 wt% tantalum, *Phys. Scr.* 2011 (2011) 14076. doi:[10.1088/0031-8949/2011/T145/014076](https://doi.org/10.1088/0031-8949/2011/T145/014076).
- [13] X. Yi, M.L. Jenkins, M.A. Kirk, Z. Zhou, S.G. Roberts, In-situ TEM studies of 150 keV W+ ion irradiated W and W-alloys: Damage production and microstructural evolution, *Acta Mater.* 112 (2016) 105–120. doi:[10.1016/j.actamat.2016.03.051](https://doi.org/10.1016/j.actamat.2016.03.051).
- [14] J. Boisse, C. Domain, C.S. Becquart, Modelling self trapping and trap mutation in tungsten using DFT and Molecular Dynamics with an empirical potential based on DFT, *J. Nucl. Mater.* 455 (2014) 10–15. doi:[10.1016/j.jnucmat.2014.02.031](https://doi.org/10.1016/j.jnucmat.2014.02.031).
- [15] F. Hofmann, D. Nguyen-Manh, M.R. Gilbert, C.E. Beck, J.K. Eliason, A.A. Maznev, W. Liu,

- D.E.J. Armstrong, K.A. Nelson, S.L. Dudarev, Lattice swelling and modulus change in a helium-implanted tungsten alloy: X-ray micro-diffraction, surface acoustic wave measurements, and multiscale modelling, *Acta Mater.* 89 (2015) 352–363. doi:10.1016/j.actamat.2015.01.055.
- [16] L. Sandoval, D. Perez, B.P. Uberuaga, A.F. Voter, Competing kinetics and the bubble morphology in W, *Phys. Rev. Lett.* 114 (2015). doi:10.1103/PhysRevLett.114.105502.
- [17] I. De Broglie, C.E. Beck, W. Liu, F. Hofmann, Temperature dependence of helium-implantation-induced lattice swelling in polycrystalline tungsten: X-ray micro-diffraction and Eigenstrain modelling, *Scr. Mater.* 107 (2015). doi:10.1016/j.scriptamat.2015.05.029.
- [18] C.E. Beck, S.G. Roberts, P.D. Edmondson, D.E.J. Armstrong, Effect of Alloy Composition & Helium ion-irradiation on the Mechanical Properties of Tungsten, Tungsten-Tantalum & Tungsten-Rhenium for Fusion Power Applications, *MRS Proc.* 1514 (2013) 99–104. doi:10.1557/opl.2013.356.
- [19] J.F. Ziegler, J. Biersack, SRIM – The stopping and range of ions in matter (2010), *Nucl. Inst. Methods Phys. Res. B.* 268 (2010) 1818–1823. doi:10.1016/j.nimb.2010.02.091.
- [20] ASTM E521–96(2009) e1, Standard Practice for Neutron Radiation Damage Simulation by Charged-Particle Irradiation, ASTM International, West Conshohocken, PA, 2009, USA., n.d.
- [21] A. Debelle, M.F.F. Barthe, T. Sauvage, First temperature stage evolution of irradiation-induced defects in tungsten studied by positron annihilation spectroscopy, *J. Nucl. Mater.* 376 (2008) 216–221. doi:10.1016/j.jnucmat.2008.03.002.
- [22] P.M. Derlet, D. Nguyen-Manh, S.L. Dudarev, Multiscale modeling of crowdion and vacancy defects in body-centered-cubic transition metals, *Phys. Rev. B - Condens. Matter Mater. Phys.* 76 (2007). doi:10.1103/PhysRevB.76.054107.
- [23] D. Nguyen-Manh, A.P. Horsfield, S.L. Dudarev, Self-interstitial atom defects in bcc transition metals: Group-specific trends, *Phys. Rev. B - Condens. Matter Mater. Phys.* 73 (2006). doi:10.1103/PhysRevB.73.020101.
- [24] W. Liu, P. Zschack, J. Tischler, G. Ice, B. Larson, X-ray laue diffraction microscopy in 3D at the advanced photon source, in: *AIP Conf. Proc.*, 2010: pp. 108–111. doi:10.1063/1.3625316.
- [25] W. Liu, G.E. Ice, B.C. Larson, W. Yang, J.Z. Tischler, J.D. Budai, The three-dimensional X-ray crystal microscope: A new tool for materials characterization, *Metall. Mater. Trans. A.* 35 (2004) 1963–1967. doi:10.1007/s11661-004-0145-1.
- [26] F. Hofmann, B. Abbey, W. Liu, R. Xu, B.F. Usher, E. Balaur, Y. Liu, X-ray micro-beam characterization of lattice rotations and distortions due to an individual dislocation., *Nat. Commun.* 4 (2013) 2774. doi:10.1038/ncomms3774.
- [27] J.W. Kysar, Y. Saito, M.S. Oztog, D. Lee, W.T. Huh, Experimental lower bounds on geometrically necessary dislocation density, *Int. J. Plast.* 26 (2010) 1097–1123. doi:10.1016/j.ijplas.2010.03.009.
- [28] C.F.O. Dahlberg, Y. Saito, M.S. Öztog, J.W. Kysar, Geometrically necessary dislocation density measurements associated with different angles of indentations, *Int. J. Plast.* 54 (2014) 81–95. doi:10.1016/j.ijplas.2013.08.008.
- [29] M.E. Kartal, R. Kiwanuka, F.P.E. Dunne, Determination of sub-surface stresses at inclusions in single crystal superalloy using HR-EBSD, crystal plasticity and inverse eigenstrain analysis, *Int. J. Solids Struct.* 67–68 (2015) 27–39. doi:10.1016/j.ijsolstr.2015.02.023.
- [30] A.J. Wilkinson, G. Meaden, D.J. Dingley, High-resolution elastic strain measurement from electron backscatter diffraction patterns: New levels of sensitivity, *Ultramicroscopy.* 106 (2006) 307–313. doi:10.1016/j.ultramicro.2005.10.001.
- [31] A.J. Wilkinson, P.B. Hirsch, Electron diffraction based techniques in scanning electron microscopy of bulk materials, *Micron.* 28 (1997) 279–308. doi:10.1016/S0968-4328(97)00032-2.
- [32] A.J. Wilkinson, Measurement of elastic strains and small lattice rotations using electron back scatter diffraction, *Ultramicroscopy.* 62 (1996) 237–247. doi:10.1016/0304-3991(95)00152-2.
- [33] S. Das, F. Hofmann, E. Tarleton, Consistent determination of geometrically necessary dislocation density from simulations and experiments, *Int. J. Plast.* (2018). doi:10.1016/j.ijplas.2018.05.001.
- [34] M. Li, D.J. Morris, S.L. Jennerjohn, D.F. Bahr, L. Levine, Finite element analysis and

- experimental investigation of the Hertzian assumption on the characterization of initial plastic yield, *J. Mater. Res.* 24 (2009) 1059–1068. doi:10.1557/jmr.2009.0134.
- [35] E.H. Lee, Elastic-Plastic Deformation at Finite Strains, *J. Appl. Mech.* 36 (1969) 1–6. <http://dx.doi.org/10.1115/1.3564580>.
- [36] F.P.E. Dunne, D. Rugg, A. Walker, Lengthscale-dependent, elastically anisotropic, physically-based hcp crystal plasticity: Application to cold-dwell fatigue in Ti alloys, *Int. J. Plast.* 23 (2007) 1061–1083. doi:10.1016/j.ijplas.2006.10.013.
- [37] G.I. Taylor, The Mechanism of Plastic Deformation of Crystals. Part I. Comparison with Observations, *Proc. R. Soc. A Math. Phys. Eng. Sci.* 145 (1934) 388–404. doi:10.1098/rspa.1934.0107.
- [38] K.M. Davoudi, J.J. Vlassak, Dislocation evolution during plastic deformation: Equations vs. discrete dislocation dynamics study, *J. Appl. Phys.* 123 (2018). doi:10.1063/1.5013213.
- [39] M.J. Makin, J. V. Sharp, A Model of Lattice Hardening in Irradiated Copper Crystals with the External Characteristics of Source Hardening, *Phys. Status Solidi.* 9 (1965) 109–118. doi:10.1002/pssb.19650090114.
- [40] C.C. Fu, F. Willaime, Ab initio study of helium in α -Fe: Dissolution, migration, and clustering with vacancies, *Phys. Rev. B - Condens. Matter Mater. Phys.* 72 (2005) 64117. doi:10.1103/PhysRevB.72.064117.
- [41] J.C. Slater, Atomic radii in crystals, *J. Chem. Phys.* 41 (1964) 3199–3204. doi:10.1063/1.1725697.
- [42] S. Das, W. Liu, R. Xu, F. Hofmann, Helium-implantation-induced lattice strains and defects in tungsten probed by X-ray micro-diffraction, *Mater. Des.* 160 (2018) 1226–1237. doi:10.1016/j.matdes.2018.11.001.
- [43] T.. Simes, S.. Mellor, D.. Hills, Research Note: A note on the influence of residual stress on measured hardness, *J. Strain Anal.* 19 (1984) 135–137. doi:https://doi.org/10.1243%2F03093247V192135.
- [44] J.. Sharp, Deformation of Neutron Irradiated Copper Alloys, *Acta Metall.* 22 (1974) 449.
- [45] J. Kacher, G. Liu, I. Robertson, In situ and tomographic observations of defect free channel formation in ion irradiated stainless steels, *Micron.* 43 (2012) 1099–1107. doi:https://doi.org/10.1016/j.micron.2012.01.017.
- [46] R. Tulluri, D.J. Morrison, Effects of ion irradiation on fatigue of Fe-12Cr-20Mn stainless steel for fusion reactor applications, *J. Mater. Eng. Perform.* 6 (1997) 454–460. doi:10.1007/s11665-997-0116-y.
- [47] S.J. Zinkle, B.N. Singh, Microstructure of neutron-irradiated iron before and after tensile deformation, *J. Nucl. Mater.* 351 (2006) 269–284. doi:https://doi.org/10.1016/j.jnucmat.2006.02.031.
- [48] N. Hashimoto, T.S. Byun, K. Farrell, S.J. Zinkle, Deformation microstructure of neutron-irradiated pure polycrystalline vanadium, *J. Nucl. Mater.* 336 (2005) 225–232. doi:https://doi.org/10.1016/j.jnucmat.2004.09.017.
- [49] N. Hashimoto, T.S. Byun, K. Farrell, S.J. Zinkle, Deformation microstructure of neutron-irradiated pure polycrystalline vanadium, *J. Nucl. Mater.* 336 (2005) 225–232. doi:https://doi.org/10.1016/j.jnucmat.2004.09.017.
- [50] T. Byun, N. Hashimoto, Strain Localization in Irradiated Materials, *Nucl. Eng. Technol.* 38 (2006) 619–638.
- [51] R.J. Wasilewski, B.C.C. stacking fault energies, *Scr. Metall.* 1 (1967) 45–47. doi:https://doi.org/10.1016/0036-9748(67)90012-9.
- [52] G.G. Slabaugh, Computing Euler angles from a rotation matrix, Denoted as TRTA Implement. from [http://www.Starfireresearch.com/services/java3dsamplecode/FlorinE Ulers Html](http://www.Starfireresearch.com/services/java3dsamplecode/FlorinE%20Users%20Html). 6 (1999) 1–6. <http://gregslabaugh.name/publications/euler.pdf>.
- [53] B.C. Larson, W. Yang, G.E. Ice, J.D. Budai, J.Z. Tischler, Three-dimensional X-ray structural microscopy with submicrometre resolution, *Nature.* 415 (2002) 887–890. doi:10.1038/415887a.
- [54] W. Liu, G.E. Ice, L. Assoufid, C. Liu, B. Shi, R. Khachatryan, J. Qian, P. Zschack, J.Z. Tischler, J.Y. Choi, Achromatic nested Kirkpatrick-Baez mirror optics for hard X-ray nanofocusing, *J. Synchrotron Radiat.* 18 (2011) 575–579. doi:10.1107/S0909049511010995.

- [55] R. Barabash, G.E. Ice, B.C. Larson, G.M. Pharr, K.S. Chung, W. Yang, White microbeam diffraction from distorted crystals, *Appl. Phys. Lett.* 79 (2001) 749–751. doi:10.1063/1.1389321.
- [56] R.I. Barabash, G.E. Ice, N. Tamura, B.C. Valek, J.C. Bravman, R. Spolenak, J.R. Patel, Quantitative analysis of dislocation arrangements induced by electromigration in a passivated interconnect, *J. Appl. Phys.* 93 (2003). doi:10.1063/1.1563033.
- [57] R.I. Barabash, G.E. Ice, *Microdiffraction Analysis of Hierarchical Dislocation Organization*, *Encycl. Mater. Technol. Updat.* Elsevier, Oxford. (2005) 1–18. http://ac.els-cdn.com/B0080431526020647/3-s2.0-B0080431526020647-main.pdf?_tid=573270f8-85f3-11e7-ac0d-00000aacb35e&acdnat=1503266764_e7fc9451b5c2dbf1485f6e13c5761bd1 (accessed August 20, 2017).
- [58] M.F. Ashby, The deformation of plastically non-homogeneous materials, *Philos. Mag.* 21 (1970) 399–424. doi:10.1080/14786437008238426.
- [59] J. Nye, Some geometrical relations in dislocated crystals, *Acta Metall.* 1 (1953) 153–162. doi:10.1016/0001-6160(53)90054-6.
- [60] A. Arsenlis, D. M. Parks, Crystallographic aspects of geometrically-necessary and statistically-stored dislocation density, *Acta Mater.* 47 (1999) 1597–1611. doi:10.1016/S1359-6454(99)00020-8.
- [61] K. Srivastava, R. Gröger, D. Weygand, P. Gumbsch, Dislocation motion in tungsten: Atomistic input to discrete dislocation simulations, *Int. J. Plast.* 47 (2013) 126–142. doi:10.1016/j.ijplas.2013.01.014.
- [62] C. Marichal, H. Van Swygenhoven, S. Van Petegem, C. Borca, {110} Slip with {112} slip traces in bcc Tungsten., *Sci. Rep.* 3 (2013) 2547. doi:10.1038/srep02547.
- [63] T.B. Britton, J.L.R. Hickey, Understanding deformation with high angular resolution electron backscatter diffraction (HR-EBSD), *IOP Conf. Ser. Mater. Sci. Eng.* 304 (2018) 12003. <http://stacks.iop.org/1757-899X/304/i=1/a=012003>.
- [64] J.A. Knapp, D.M. Follstaedt, J.C. Barbour, S.M. Myers, Finite-element modeling of nanoindentation for determining the mechanical properties of implanted layers and thin films, *Nucl. Instruments Methods Phys. Res. Sect. B Beam Interact. with Mater. Atoms.* 127–128 (1997) 935–939. doi:[https://doi.org/10.1016/S0168-583X\(97\)00034-7](https://doi.org/10.1016/S0168-583X(97)00034-7).
- [65] G.M. Pharr, W.C. Oliver, Measurement of Thin Film Mechanical Properties Using Nanoindentation, *MRS Bull.* 17 (1992) 28–33. doi:10.1557/S0883769400041634.
- [66] W.D. Nix, Elastic and plastic properties of thin films on substrates: nanoindentation techniques, *Mater. Sci. Eng. A.* 234–236 (1997) 37–44. doi:[https://doi.org/10.1016/S0921-5093\(97\)00176-7](https://doi.org/10.1016/S0921-5093(97)00176-7).
- [67] H. Ogiwara, A. Kohyama, H. Tanigawa, H. Sakasegawa, Irradiation-induced hardening mechanism of ion irradiated JLF-1 to high fluences, *Fusion Eng. Des.* 81 (2006) 1091–1097. doi:<https://doi.org/10.1016/j.fusengdes.2005.09.063>.
- [68] C. Heintze, C. Recknagel, F. Bergner, M. Hernández-Mayoral, A. Kolitsch, Ion-irradiation-induced damage of steels characterized by means of nanoindentation, *Nucl. Instruments Methods Phys. Res. Sect. B Beam Interact. with Mater. Atoms.* 267 (2009) 1505–1508. doi:<https://doi.org/10.1016/j.nimb.2009.01.122>.
- [69] M. Ando, H. Tanigawa, S. Jitsukawa, T. Sawai, Y. Katoh, A. Kohyama, K. Nakamura, H. Takeuchi, Evaluation of hardening behaviour of ion irradiated reduced activation ferritic/martensitic steels by an ultra-micro-indentation technique, *J. Nucl. Mater.* 307–311 (2002) 260–265. doi:[https://doi.org/10.1016/S0022-3115\(02\)01250-3](https://doi.org/10.1016/S0022-3115(02)01250-3).
- [70] F.H. Featherston, J.R. Neighbours, Elastic constants of tantalum, tungsten, and molybdenum, *Phys. Rev.* 130 (1963) 1324–1333. doi:10.1103/PhysRev.130.1324.
- [71] D.I. Bolef, J. De Klerk, Elastic Constants of Single-Crystal Mo and W between 77° and 500°K, *J. Appl. Phys.* 33 (1962) 2311–2314. doi:10.1063/1.1728952.
- [72] C.A. Klein, G.F. Cardinale, Young’s modulus and Poisson’s ratio of CVD diamond, *Diam. Relat. Mater.* 2 (1993) 918–923. http://ac.els-cdn.com/0925963593902506/1-s2.0-0925963593902506-main.pdf?_tid=634b8a44-66f1-11e7-8022-00000aab0f27&acdnat=1499857439_c559947dc1faf69566a6282716d3b8e2 (accessed July 12, 2017).

- [73] R.A. Ayres, G.W. Shannette, D.F. Stein, S.G. Roberts, T. Ahlgren, S. Antusch, D.E.J. Armstrong, M. Balden, N. Baluc, M.-F. Barthe, W.W. Basuki, M. Battabyal, C.S. Becquart, D. Blagoeva, H. Boldryeva, J. Brinkmann, M. Celino, L. Ciupinski, J.B. Correia, A. De Backer, C. Domain, E. Gaganidze, C. García-Rosales, J. Gibson, M.R. Gilbert, S. Giusepponi, B. Gludovatz, H. Greuner, K. Heinola, T. Höschen, A. Hoffmann, N. Holstein, F. Koch, W. Krauss, H. Li, S. Lindig, J. Linke, C. Linsmeier, P. López-Ruiz, H. Maier, J. Matejcek, T.P. Mishra, M. Muhammed, A. Muñoz, M. Muzyk, K. Nordlund, D. Nguyen-Manh, J. Opschoor, N. Ordás, T. Palacios, G. Pintsuk, R. Pippa, J. Reiser, J. Riesch, S.G. Roberts, L. Romaner, M. Rosiński, M. Sanchez, W. Schulmeyer, H. Traxler, A. Ureña, J.G. van der Laan, L. Veleva, S. Wahlberg, M. Walter, T. Weber, T. Weitkamp, S. Wurster, M.A. Yar, J.H. You, A. Zivelonghi, Elastic constants of tungsten–rhenium alloys from 77 to 298 °K, *J. Appl. Phys.* 46 (1975) 1526–1530. doi:10.1063/1.321804.
- [74] B.N. Dutta, B. Dayal, Lattice Constants and Thermal Expansion of Palladium and Tungsten up to 878 C by X-Ray Method, *Phys. Status Solidi.* 3 (1963) 2253–2259. doi:10.1002/pssb.19630031207.
- [75] C.A. Sweeney, W. Vorster, S.B. Leen, E. Sakurada, P.E. McHugh, F.P.E. Dunne, The role of elastic anisotropy, length scale and crystallographic slip in fatigue crack nucleation, *J. Mech. Phys. Solids.* 61 (2013) 1224–1240. doi:10.1016/j.jmps.2013.01.001.
- [76] A. Cottrell, *An introduction to metallurgy*, Universities Press, 1990.
- [77] D. Cereceda, J. Marian, J. Marian, Nudged Elastic Band Simulations of Kink Pairs in Tungsten, 2015. <https://e-reports-ext.llnl.gov/pdf/787753.pdf>.
- [78] C.R. Weinberger, B.L. Boyce, C.C. Battaile, Slip planes in bcc transition metals, *Int. Mater. Rev.* 58 (2013) 296–314. doi:10.1179/1743280412Y.0000000015.
- [79] G. Po, Y. Cui, D. Rivera, D. Cereceda, T.D. Swinburne, J. Marian, N. Ghoniem, A phenomenological dislocation mobility law for bcc metals, *Acta Mater.* 119 (2016) 123–135. doi:10.1016/j.actamat.2016.08.016.
- [80] G.D. Samolyuk, Y.N. Osetsky, R.E. Stoller, The influence of transition metal solutes on the dislocation core structure and values of the Peierls stress and barrier in tungsten, *J. Phys. Condens. Matter.* 25 (2013). doi:10.1088/0953-8984/25/2/025403.
- [81] NIST Chemistry Web book, SRD69, Natl. Inst. Stand. Technol. (n.d.). <https://webbook.nist.gov/cgi/cbook.cgi?ID=C7440337&Mask=2>.
- [82] S.L. Dudarev, P.-W. Ma, Elastic fields, dipole tensors, and interaction between self-interstitial atom defects in bcc transition metals, *Phys. Rev. Mater.* 2 (2018) 33602. doi:10.1103/PhysRevMaterials.2.033602.